The Astrophysical Journal, 937:112 (16pp), 2022 October 1 https://doi.org/10.3847/1538-4357/ac8b83

Resolving the Peak of the Black Hole Mass Spectrum

Ebraheem Farag[1,2], Mathieu Renzo[3], Robert Farmer[4], Morgan T. Chidester[1,2], and F. X. Timmes[1,2]
[1] School of Earth and Space Exploration, Arizona State University, Tempe, AZ 85287, USA; ekfarag@asu.edu
[2] Joint Institute for Nuclear Astrophysics—Center for the Evolution of the Elements, USA
[3] Center for Computational Astrophysics, Flatiron Institute, New York, NY 10010, USA
[4] Max-Planck-Institut für Astrophysik, Karl-Schwarzschild-Straße 1, D-85741 Garching, Germany
Received 2022 June 27; revised 2022 August 15; accepted 2022 August 18; published 2022 October 4

Abstract

Gravitational-wave (GW) detections of binary black hole (BH) mergers have begun to sample the cosmic BH mass distribution. The evolution of single stellar cores predicts a gap in the BH mass distribution due to pair-instability supernovae (PISNe). Determining the upper and lower edges of the BH mass gap can be useful for interpreting GW detections of merging BHs. We use MESA to evolve single, nonrotating, massive helium cores with a metallicity of $Z = 10^{-5}$, until they either collapse to form a BH or explode as a PISN, without leaving a compact remnant. We calculate the boundaries of the lower BH mass gap for S-factors in the range S(300 keV) = (77,203) keV b, corresponding to the $\pm 3\sigma$ uncertainty in our high-resolution tabulated $^{12}C(\alpha,\gamma)^{16}O$ reaction rate probability distribution function. We extensively test temporal and spatial resolutions for resolving the theoretical peak of the BH mass spectrum across the BH mass gap. We explore the convergence with respect to convective mixing and nuclear burning, finding that significant time resolution is needed to achieve convergence. We also test adopting a minimum diffusion coefficient to help lower-resolution models reach convergence. We establish a new lower edge of the upper mass gap as $M_{\rm lower} \simeq 60^{+32}_{-14}\ M_\odot$ from the $\pm 3\sigma$ uncertainty in the $^{12}C(\alpha, \gamma)^{16}O$ rate. We explore the effect of a larger 3α rate on the lower edge of the upper mass gap, finding $M_{\rm lower} \simeq 69^{+34}_{-18}\ M_\odot$. We compare our results with BHs reported in the Gravitational-Wave Transient Catalog.

Unified Astronomy Thesaurus concepts: Gravitational waves (678); Black holes (162); Nuclear astrophysics (1129); Stellar physics (1621); Core-collapse supernovae (304)

1. Introduction

The black hole (BH) initial mass function from single-star evolutionary models predicts three physics-driven transitions in the distribution. In order of increasing mass, the first transition is set by the maximum possible neutron star mass; the second by electron–positron pair production from energetic photons in the stellar interior of a massive star; and the third by exothermic photodisintegration reactions, which absorb enough energy in a high-temperature stellar core for the model star to, once again, reach core collapse (CC).

In the first transition, the maximum observed masses of neutron stars include about $2.01\,M_\odot$ for PSR J0348+0432 (Antoniadis et al. 2013), about 2.08–$2.14\,M_\odot$ for PSR J0740 +6620 (Cromartie et al. 2020; Farr & Chatziioannou 2020; Fonseca et al. 2021; Miller et al. 2021; Riley et al. 2021), and about $2.16\,M_\odot$ for GW170817 (Abbott et al. 2017a, 2017b; Rezzolla et al. 2018). The integration of the general relativistic equations of hydrostatic equilibrium with a nuclear equation of state predicts a restricted range of allowed gravitational neutron star masses, with the currently favored equations of state giving $\simeq$0.1–$2.5\,M_\odot$ (Banik et al. 2014; Marques et al. 2017; Ferreira & Providencia 2021; Lattimer 2021). The lower bound is the minimum stable neutron star mass (Oppenheimer & Serber 1938; Colpi et al. 1989; Haensel et al. 2002; Koliogiannis & Moustakidis 2021), although a more relevant minimum mass stems from a neutron star's origin in a supernova (Timmes et al. 1996; Zhang et al. 2008; Sukhbold et al. 2016; Richers et al. 2017; Sukhbold et al. 2018; Ghosh et al. 2022; Patton et al. 2022) or the accretion-induced collapse of a white dwarf (Fryer et al. 1999; Schwab 2021; Wang et al. 2022). Less massive neutron star masses can undergo explosive decompression (Page 1982; Colpi et al. 1993; Sumiyoshi et al. 1998; Nixon et al. 2020), while more massive ones overcome the repulsive strong force and neutron degeneracy pressure to collapse into BHs.

In addition, there is an apparent paucity of observed BH candidates in the $\simeq$2.5–$5\,M_\odot$ mass range (Bailyn et al. 1998; Ozel et al. 2010; Belczynski et al. 2012), hinting at the possible existence of a contested "lower mass gap" (Farr et al. 2011; Wyrzykowski & Mandel 2020; Zevin et al. 2020; Mandel & Farmer 2022). The "lower edge" of the lower mass gap is set by the maximum possible neutron star mass, while the "upper edge" is set by the minimum observed BH mass. The upper edge of the lower mass gap, if it exists, is currently uncertain, as the BHs found in this mass range may have been created by changes in the growth time of convection during an SN explosion (Fryer et al. 2022) or by binary neutron star mergers (Thompson et al. 2019; Abbott et al. 2020; Gupta et al. 2020; Yang et al. 2020; Ye & Fishbach 2022).

The second and third transitions form the "upper mass gap"—see Figure 1. Models with zero-age main-sequence (ZAMS) masses $M_{\rm ZAMS} \gtrsim 100\,M_\odot$ reach central temperatures of $T_c \gtrsim 7 \times 10^8$ K. This allows for the production of electron–positron pairs from photons, $\gamma+\gamma \rightarrow e^- + e^+$, which soften the equation of state (Fowler & Hoyle 1964; Barkat et al. 1967; Rakavy & Shaviv 1967). These models become dynamically unstable before core O depletion, as the pair production leads to regions where the adiabatic index $\Gamma_1 \leqslant 4/3$ (Fraley 1968; Ober et al. 1983; Bond et al. 1984).

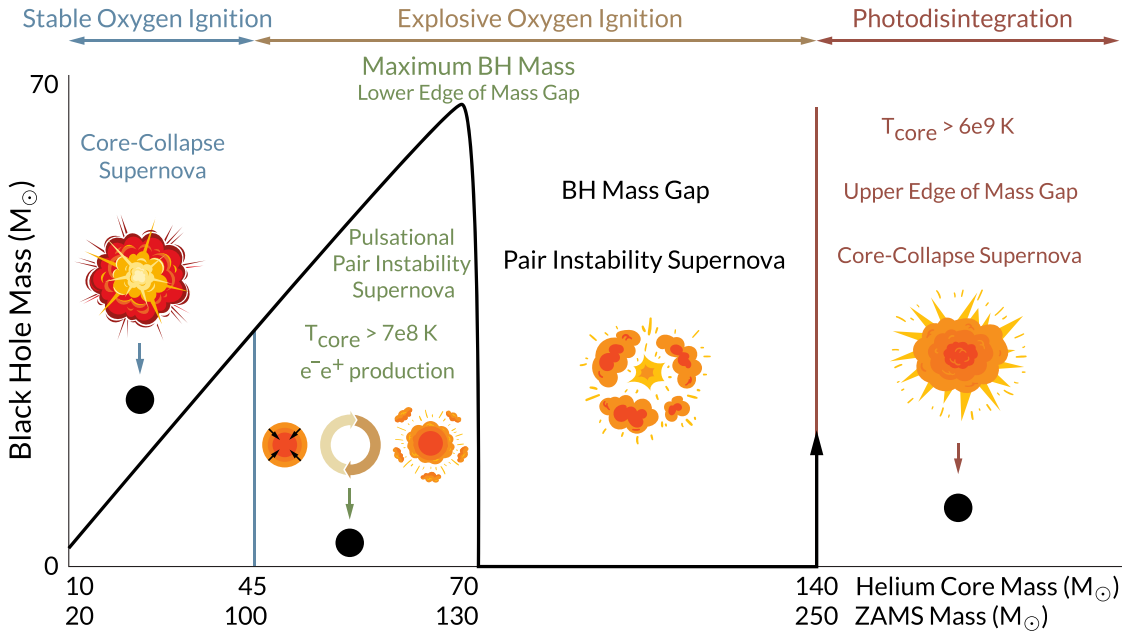

Figure 1. Illustration of a single-star BH mass spectrum.

The ensuing dynamical collapse results in explosive O burning, with a variety of possible outcomes (Glatzel et al. 1985; Woosley et al. 2002; Heger et al. 2003; Takahashi 2018; Farmer et al. 2019; Marchant et al. 2019; Marchant & Moriya 2020; Renzo et al. 2020a; Woosley & Heger 2021; Mehta et al. 2022; Renzo et al. 2022). The energy injected can cause a cyclic pattern of entering the pair-instability region, contracting, burning, and expanding, eventually leading to pulsational pair-instability supernovae (PPISNe) and a BH remnant. The energy injected by a single strong pulse can also unbind the model, without leaving a BH remnant in a pair-instability supernova (PISN). This transition to a PISN defines the "lower edge" of the upper mass gap. Models with $M_{\rm ZAMS} \gtrsim 250\,M_\odot$ reach $T_c \gtrsim 6 \times 10^9$ K, where endothermic photodisintegration reactions absorb enough energy to prevent the star from unbinding (Bond et al. 1984; Heger et al. 2003). This third transition defines the "upper edge" of the upper mass gap.

The ZAMS masses of the second and third transitions depend on the He core-to-ZAMS mass mapping, and thus on the rotation, convective boundary mixing, and mass loss adopted (Vink et al. 2015; Woosley 2019; Higgins et al. 2021; Vink et al. 2021). Since roughly half of all massive stars are found in binaries (Sana & Evans 2011; Sana et al. 2012), a simple assumption is that binary interactions will strip the H envelope, revealing bare He cores, before He burning commences. This can occur from Roche lobe overflow and/or the formation and ejection of a common envelope. All low-metallicity stars, including those with H-rich envelopes, are also expected to explode as PPISN/PISN, and lose part or all of their envelope in the pulses (Woosley 2017; Renzo et al. 2020b). As we are only interested in determining the peak BH masses from gravitational-wave (GW) sources in isolated systems, we assume that their progenitors are He cores.

While the three transitions are set by nuclear and particle physics, the total number of BHs, as well as their distribution with mass, is a consequence of stellar evolution. A number of uncertain factors make a straightforward determination challenging. For example, current estimates of the BH initial mass function from single stars chiefly rely on parameterized explosion models (Fryer et al. 2012; Spera et al. 2015; Patton & Sukhbold 2020; Zapartas et al. 2021; Fryer et al. 2022; Patton et al. 2022; Renzo et al. 2022). Models for the evolution from the ZAMS also still rely on effective mixing length theories for convection, including ours. Finally, the BHs in either mass gap may occur through mechanisms other than those involving a single star. Examples include isolated binary star evolution (de Mink & Mandel 2016; Spera et al. 2019; Belczynski 2020; Breivik et al. 2020; van Son et al. 2020; Santoliquido et al. 2021; Fuller & Lu 2022), dynamical formation in dense star clusters (Portegies Zwart & McMillan 2000; Di Carlo et al. 2020; Renzo et al. 2020a; Fragione et al. 2022), mergers in higher-multiplicity systems (Antonini & Perets 2012; Liu & Lai 2018; Hamers & Samsing 2019), mergers of compact binaries in galactic nuclei (O'Leary et al. 2009; Bartos et al. 2017; Wang et al. 2021), and mass loss from putative progenitors above the PISN regime (i.e., super-kilonovae; Siegel et al. 2021). Contributions from the different populations may be unraveled as the number of detected GW events increases (Perna et al. 2019; Renzo et al. 2021; Zevin et al. 2021; Mandel & Broekgaarden 2022).

This article focuses on the second transition—the lower edge of the upper mass gap. The predicted BH masses at the lower edge from single naked He core models are generally robust with respect to the model uncertainties (Takahashi 2018; Farmer et al. 2019; Farmer et al. 2020; Marchant & Moriya 2020; Renzo et al. 2020c), but depend sensitively on the $^{12}C(\alpha,\gamma)^{16}O$ reaction rate (Farmer et al. 2020). The masses and spins of merging binary black holes (BBHs) from LIGO/Virgo/Karga (LVK; Acernese et al. 2015; LIGO Scientific Collaboration et al. 2015; Akutsu et al. 2021) observations probe the location of the lower edge of the upper mass gap. The observed lower edge can then be used to place a constraint on the $^{12}C(\alpha,\gamma)^{16}O$ reaction rate (Farmer et al. 2020). However, we caution that LVK merging BHs might have a very complex astrophysical history (e.g., binary evolution and stellar dynamics), which might blur the mass gap, so that the mass gap may not appear at all with the LVK BHs. Furthermore, we

caution that there are competing effects at the lower edge of the mass gap (e.g., overshooting and the collapse of the H envelope) that might have the same effect as varying the $^{12}C(\alpha,\gamma)^{16}O$ reaction rate.

The main novelty of this article is a new effort, initiated by Farmer et al. (2020) and refined in Mehta et al. (2022), that aims to show convergence in the sequence of models used to define the lower edge of the upper mass gap as a function of the He burning reaction rates. Section 2 describes our models, Sections 3 and 4 describe our results, and Section 5 summarizes our conclusions.

2. Models

We use MESA version r11701 to evolve single nonrotating massive He cores with a metallicity of $Z = 10^{-5}$, until they either collapse to form a BH or explode as a PISN, without leaving a compact remnant. We adopt a low metallicity, so that stellar winds are irrelevant (Farmer et al. 2019), to avoid the possible numerical complications of resolving models with winds (Renzo et al. 2017). Low-metallicity environments are also likely to form some of the most massive stellar-mass BHs that can be detected as GW sources (Mapelli 2021; Vink et al. 2021; Mandel & Farmer 2022; Spera et al. 2022). Metallicities as low as $Z = 0.02\,Z_\odot$ are enough to yield final He core masses of up to $140\,M_\odot$, when adopting the recently updated and physically motivated Wolf–Rayet mass-loss schemes (Higgins et al. 2021).

We use the same MESA inlists and run_star_extras.f90 as used in Farmer et al. (2020) and Mehta et al. (2022) to calculate the BH mass spectrum across the lower edge of the upper mass gap. We also use a 21-isotope nuclear network with nuclear reaction rates from the NACRE compilation (Angulo et al. 1999) and the JINA reaclib database (Cyburt et al. 2010). The tabulated $^{12}C(\alpha,\gamma)^{16}O$ reaction rates were originally provided by deBoer et al. (2017) and refined in Mehta et al. (2022). A total of 1750 models were run, which consumed ≃3,000,000 core hours. Full details of the MESA models and the reaction rate files, to reproduce our results, are available online.[5]

Preceding any individual pulse, we use MESA's implicit hydrodynamic solver. As a model evolves into the pair-instability region, we switch to MESA's Harten–Lax–van Leer–Contact (HLLC) hydrodynamic solver (Toro et al. 1994; Paxton et al. 2018) to resolve the shocks during the dynamic phase of evolution. The switch generally occurs when the central temperatures exceed 10^9 K and the volumetric pressure-weighted average adiabatic index $\langle\Gamma_1\rangle - 4/3 < 0.01$ (Stothers 1999; Farmer et al. 2019; Marchant et al. 2019). We then follow the core as it gravitationally unbinds on the first pulse as a PISN, or contracts and rebounds repeatedly until all shocks have reached the surface of the model (Yoshida et al. 2016; Woosley 2017; Marchant et al. 2019; Renzo et al. 2020c). Individual pulses can eject between $\simeq 0.01\,M_\odot$ and $\simeq 30\,M_\odot$, with surface velocities up to 20,000 km s^{-1}.

Once hydrostatic equilibrium is reached again, the unbound material is removed and the remaining mass is relaxed to a new stellar model, with an identical entropy and chemical profile. This is possible because the removed mass is already moving at speeds beyond both the escape velocity and the surface sound speed, so no backreaction on the remaining material is expected (Marchant et al. 2019). The evolution then continues with the implicit solver. The new model contracts as it loses energy, due to radiation and neutrino emission, until it undergoes an additional pulse or collapses to form a BH. At the onset of CC, the HLLC solver is activated to capture the dynamics of the infalling core. We define CC as occurring when any part of the model begins to collapse with velocities $v > 8000$ km s^{-1}, so as to capture any pulse that might be ejected during CC. The mass of the BH is defined as the mass of the bound material at CC (Renzo et al. 2020c). These BH masses are upper limits, due to the uncertainties in BH formation (Fryer et al. 2001; Branch & Wheeler 2017; Uchida et al. 2019; Mandel & Broekgaarden 2022; Renzo et al. 2022) and weak shock generation (Nadyozhin 1980; Fernandez et al. 2018; Ivanov & Fernandez 2021; Rahman et al. 2022).

3. Convergence of the Peak BH Mass Spectrum

Mapping the final evolutionary phases of massive stars remains challenging, given the difficulty in resolving the interplay between convection, nuclear burning, rotation, convective core overshooting, radiative transport, internal waves, mass-loss eruptions, and binary interactions (Quataert & Shiode 2012; Shiode & Quataert 2014; Matzner & Ro 2021; Tanikawa et al. 2021; Vink et al. 2021; Jacobson-Galan et al. 2022; Wu & Fuller 2022). All else being equal, mass resolution is an important consideration to accurately control for changes in stellar structure (Farmer et al. 2016). Assessing the sensitivity to mass resolution is a necessary practice for ensuring robust predictions. The evolutions of PPISN stars are characterized by short episodes of strong nuclear burning in their core, rapidly changing their composition and density. We will control changes in the central density for temporal resolution. PPISN stars also eject large amounts of material at and beneath escape velocity. We will control the spatial mesh resolution of our models to resolve this material.

The goal of this section is to assess the numerical convergence of the MESA models used to determine the lower edge of the upper mass gap, with respect to spatial and temporal resolutions. During hydrostatic phases of evolution, when the implicit solver is active, we control the number of cells with max_dq, the maximum fractional mass in a cell. That is, the minimum number of cells is 1/max_dq. During the dynamic phases of evolution, when the HLLC solver is active, we control the number of cells with split_merge_amr_nz_baseline. For both phases of evolution, we primarily control the time step with delta_lgRho_cntr_limit, which limits the time step such that the change in the logarithm of the central density is less than a specified fraction.

In the following sections, we indicate a "strong" pulse as a single pulse that arises from $\langle\Gamma_1 - 4/3\rangle < 0$ and results in the ejection of $>0.1\,M_\odot$ of material. We indicate "weak" pulses as any rebounding pulses that are formed while the model relaxes from a strong pulse. Weak pulses also arise at or just above $\langle\Gamma_1 - 4/3\rangle = 0$, from dynamical behavior that is not strong enough to remove $>0.1\,M_\odot$ of material with a single shock, yet can remove $\gg 0.1\,M_\odot$ in a series of several significantly weaker pulses, which compound the shocks near the surface. Strong pulses typically develop on a timescale of $\leqslant 50$ s, while typical periods for the contraction and bounce of a single weak pulse can range between, but are not limited to, 10^2–10^3 s. In this paper, a PPISN is any model in which a single strong pulse or a series of weak pulses is able to remove $\geqslant 0.1\,M_\odot$ of material

[5] doi: 10.5281/zenodo.6930577

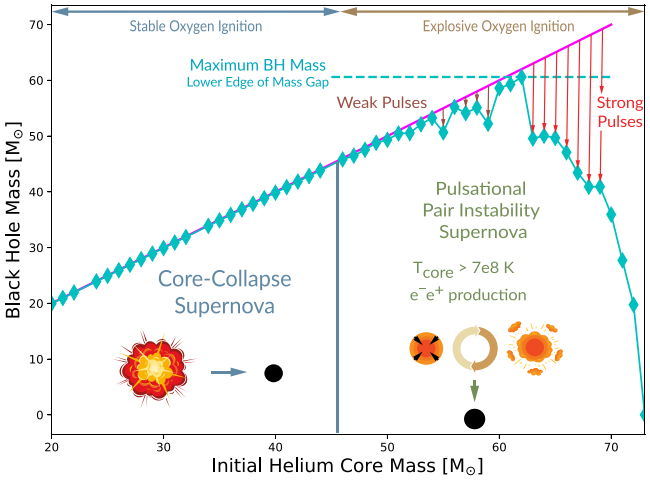

Figure 2. The same as Figure 1, but with an example of a calculated BH mass spectrum (the teal line and diamonds). The magenta line marks $M_{\rm BH} = M_{\rm He}$. The peak BH mass is labeled. The smaller masses, just to the left of the peak, show weak pulses. The larger masses, just to the right, show strong pulses.

from the surface. Figure 2 illustrates a sample BH mass spectrum with weak and strong pulses.

3.1. Global Mixing Floors

Because of the finite size of the Lagrangian mesh representing a star in numerical models, sharp gradients (e.g., in chemical composition or thermal properties) can be hard to resolve. This can lead to unphysical "spikes," which can have an oversized and resolution-dependent effect on stellar processes, depending on those gradients (e.g., mixing instabilities). To mitigate this effect, a global minimum chemical mixing diffusion coefficient $D_{\rm min}$ can be used. Physically, $D_{\rm min}$ may be interpreted as a small amount of mixing arising from small-scale perturbations that are not captured in 1D models. The global evolution of a model is unaffected when the associated diffusive mixing timescale $\tau = L^2/D_{\rm min}$—where L is the characteristic length scale over which the mixing is active—is significantly longer than the lifetime of the stellar model. Choosing $D_{\rm min} = 10^{-2}$ cm^2 s^{-1}, `min_D_mix` in `MESA`, and a typical PPISN radius of $R_{\rm He} = 1$–$10\,R_\odot$, the global mixing timescale is $\tau \simeq 10^{17}$ yr. A $50\,M_\odot$ He core has a lifetime of $\simeq 10^5$ yr, about 12 orders of magnitude smaller than this global mixing timescale. Thus, we do not anticipate a significant *global* impact with this value of $D_{\rm min}$, while it smooths *local* composition gradients. Nevertheless, models at the boundaries of different physical behaviors (e.g., CC or pulsational pair-instability) may differ qualitatively.

Figures 3 and 4 illustrate the difference in evolutionary behavior between three $M_{\rm He} = 50\,M_\odot$ models, from the advent of shell C burning to CC. The thermal evolution of these models is dominated by neutrino cooling, and therefore all three models remain in local thermodynamic equilibrium. Figure 3 compares the luminosities, timescales, energies, and integrated $\langle \Gamma_1 - 4/3 \rangle$ of three $50\,M_\odot$ He core models, as they evolve to CC. Figure 4 displays the convective and nuclear burning behavior of these models. Model 1 uses the same mass and temporal resolutions as Farmer et al. (2020):

`max_dq` = 1d-3
`split_merge_amr_nz_baseline` = 6000
`delta_lgRho_cntr_limit` = 2.5d-3
`min_D_mix` = 0.

Model 1 uses ≃2000–3000 cells during the hydrostatic phases, ≃2500–3500 cells during the dynamic phases, and ≃13,000 time steps to reach CC. Model 2 is the same as Model 1, but sets `min_D_mix`=1d-2. Model 2 uses ≃2000–3000 cells during the hydrostatic phases, ≃2500–4200 cells during the dynamic phases, and ≃9000 time steps to reach CC. Model 3 is the same as Model 1, but with about twice the mass resolution and 25 times the temporal resolution:

`max_dq` = 2d-4
`split_merge_amr_nz_baseline` = 12000
`delta_lgRho_cntr_limit` = 1d-4
`min_D_mix` = 0.

Model 3 uses ≃3500–4000 cells during the hydrostatic phases, ≃5000–10,000 cells during the dynamic phases, and ≃740,000 time steps to reach CC.

In models 1, 2, and 3, off-center C ignition occurs at log $(t_{\rm cc} - t) \simeq 7.4$, log $(t_{\rm cc} - t) \simeq 6.5$, and log $(t_{\rm cc} - t) \simeq 6.4$. In model 1, the chemical evolution of the core is interrupted by a dynamical episode at log $(t_{\rm cc} - t) \simeq 7.3$. Shell C burning is an insufficient energy source for combating the dynamical instability, as only a fraction of the ^{12}C in the shell that is burned before Γ_1 instability leads to a core contraction. During this contraction, the He-burning shell propagates inward, mixing and burning alongside Ne, Mg, and Si in the O-rich shell, stabilizing the core until CC.

Models 2 and 3 smoothly evolve through shell C burning, and undergo weak dynamical behavior and a steady decrease in total energy, as their cores smoothly evolve toward CC. With $D_{\rm min} = 10^{-2}$ cm^2 s^{-1}, model 2 experiences minimal mixing between the He-rich shell and the C–O core, commensurate with model 3. Models 2 and 3 both smoothly burn through most of the ^{12}C in the C–O shell, while their cores burn through oxygen. This convective C-burning shell stabilizes the star long enough to prevent a dynamical contraction that disrupts the core burning, unlike model 1. When the mass fraction of carbon, $X(^{12}{\rm C})$, in the shell drops below $\sim 10^{-2}$, the shell burning is no longer strong enough to prevent Γ_1 instability from pair production. The shell begins to contract from the outside inward, rebounding off the core from brief episodes of explosive O burning. These explosive burning episodes drive weak shocks outward, momentarily stabilizing the shell until the shocks reach the surface and the shell contracts again. During each contraction, the temperatures and densities increase, causing the Ne and Mg burning in the outer shell to reach deeper inside the model with each contraction, then recede back toward the surface during each pulse. As the core evolves further toward CC, the Si burning contributes to each episode. These pulsations can be seen in the oscillations of $\langle \Gamma_1 - 4/3 \rangle$ and the oscillatory convection in Figures 3 and 4. Model 2 manages to resolve a few pulsations before CC, each ejecting a small amount of mass, resulting in $M_{\rm eject} \simeq 0.01\,M_\odot$. The higher resolution of model 3 is able to resolve >140 pulses before reaching CC, with each pulse releasing a small amount of mass, resulting in $M_{\rm eject} \simeq 0.45\,M_\odot$.

Adopting $D_{\rm min} = 10^{-2}$ cm^2 s^{-1} improves the rate of numerical convergence of low-resolution models, akin to a slight increase in temporal resolution. While model 2 can resolve the core burning reasonably well, the time steps are too large to fully resolve the nuclear burning in the shell or the coupling between the core and the shell that generates

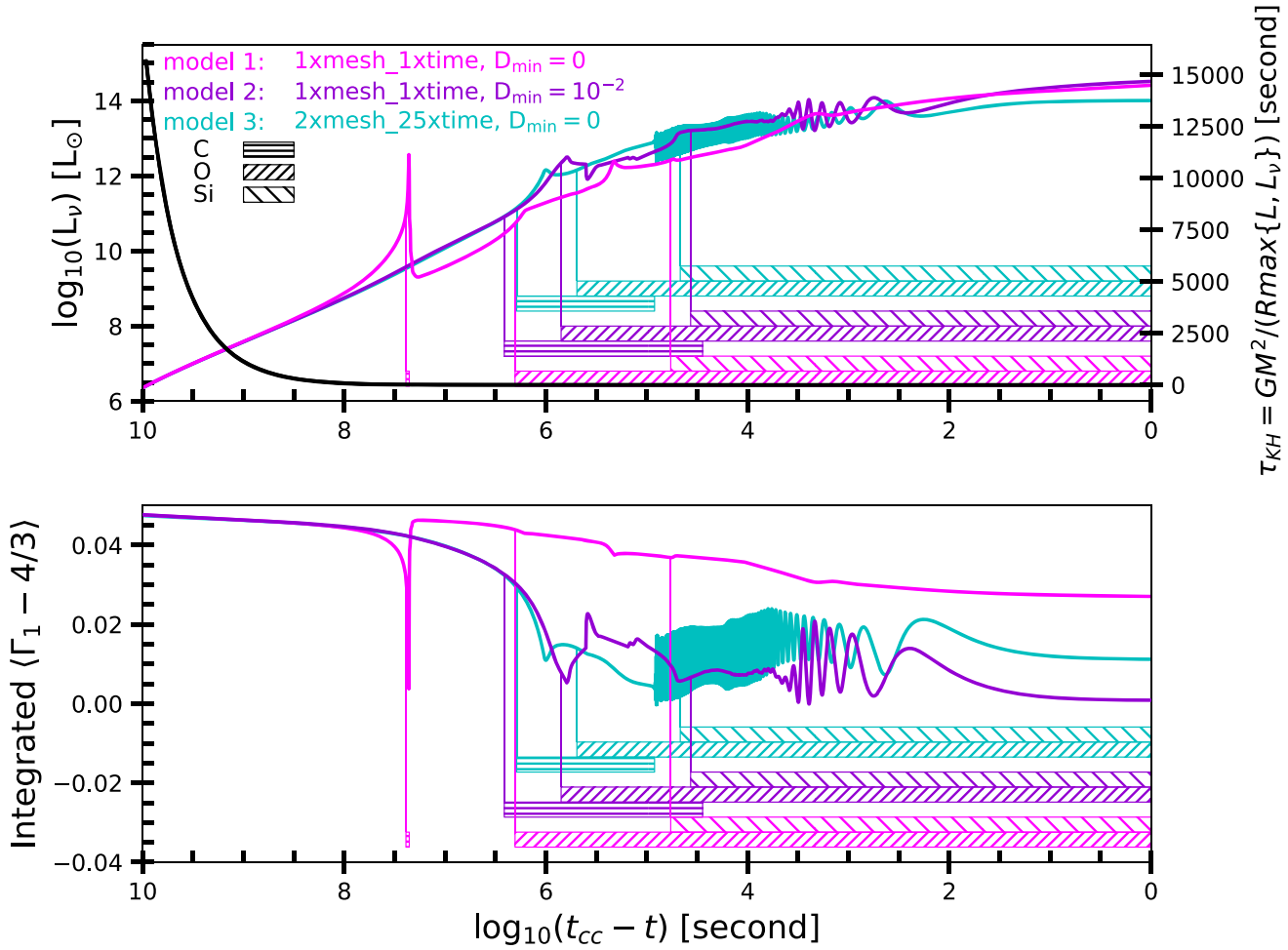

Figure 3. Both panels share the same x-axis, the logarithmic time to CC, in seconds. The top panel shows the neutrino luminosity and the Kelvin–Helmholtz timescale, normalized to account for the energy lost to neutrinos, which dominates over photon cooling in the evolutionary phases shown. The integrated $\langle \Gamma_1 - 4/3 \rangle$ is shown in the bottom panel, to illustrate when the models are evolving dynamically. The hatched regions indicate where the C shell, O core, and Si core burning take place.

oscillatory burning in the core during later stages, as in model 3. Because our time steps are primarily limited by `delta_lgRho_cntr_limit`, small changes in the central density resulting from the dynamical contraction between each core and shell-burning episode can be fully resolved in model 3, but not in models 1 or 2. Only the strongest, largest core–shell contractions can be resolved at the lower resolution of model 2. Since each contraction does not change the core density by an appreciably large level, the time steps taken by model 2 skip or smooth over many of these pulsations. This suggests that $D_{\rm min} = 10^{-2}$ cm^2 s^{-1} improves the rate of convergence of models run with lower resolution, but cannot fully recover the convective behavior generated by models that use significantly greater temporal resolution. Next, we continue our exploration of $D_{\rm min} = 10^{-2}$ cm^2 s^{-1} at higher resolution, to better characterize the impact across the entire BH mass spectrum.

3.2. Resolution Testing the Single-star BH Mass Spectrum

In Farmer et al. (2019), Marchant et al. (2019), Renzo et al. (2020a), and Mehta et al. (2022), brief explorations of enhanced mass and temporal resolutions were conducted, but further work was needed to assess the convergence of these models across the entire BH mass spectrum. In this section, we take on the challenge of exploring the numerical convergence of the `MESA` stellar models computed across the BH mass spectrum. The goal of this section is to achieve convergence in the peak BH mass at the $<1\,M_\odot$ level. We focus on resolution testing the BH mass spectrum for He cores with the $\sigma = 0$ ^{12}C(α,γ)^{16}O reaction rate provided by deBoer et al. (2017), updated to the 2015 temperature points in Mehta et al. (2022), corresponding to an approximate astrophysical S-factor S(300 keV) = 140 keV b. We also investigate the inclusion of a minimum diffusive mixing floor $D_{\rm min}$ on the BH mass spectrum.

Our testing consists of 16 different model resolutions, each modified using some variation of `max_dq`, `split_merge_amr_nz_baseline`, and `delta_lgRho_cntr_limit`, to control for mass and temporal resolutions. In Table 1, we summarize the adopted resolutions and associated peak BH spectra masses. In Figure 5, we plot the BH mass spectrum for each resolution listed in Table 1. The baseline resolution of `1m_1h_1t` represents the resolution adopted in Farmer et al. (2020). All other models are scaled up from `1m_1h_1t`. Generally, models with `1m`, `2m`, and `5m` have between 2000–3000, 3500–4000, and 7000–8000 cells, respectively, during the hydrostatic phase of evolution. Models with `1h`, `2h`, and `5h` have between 2500–4500, 5000–10,000,

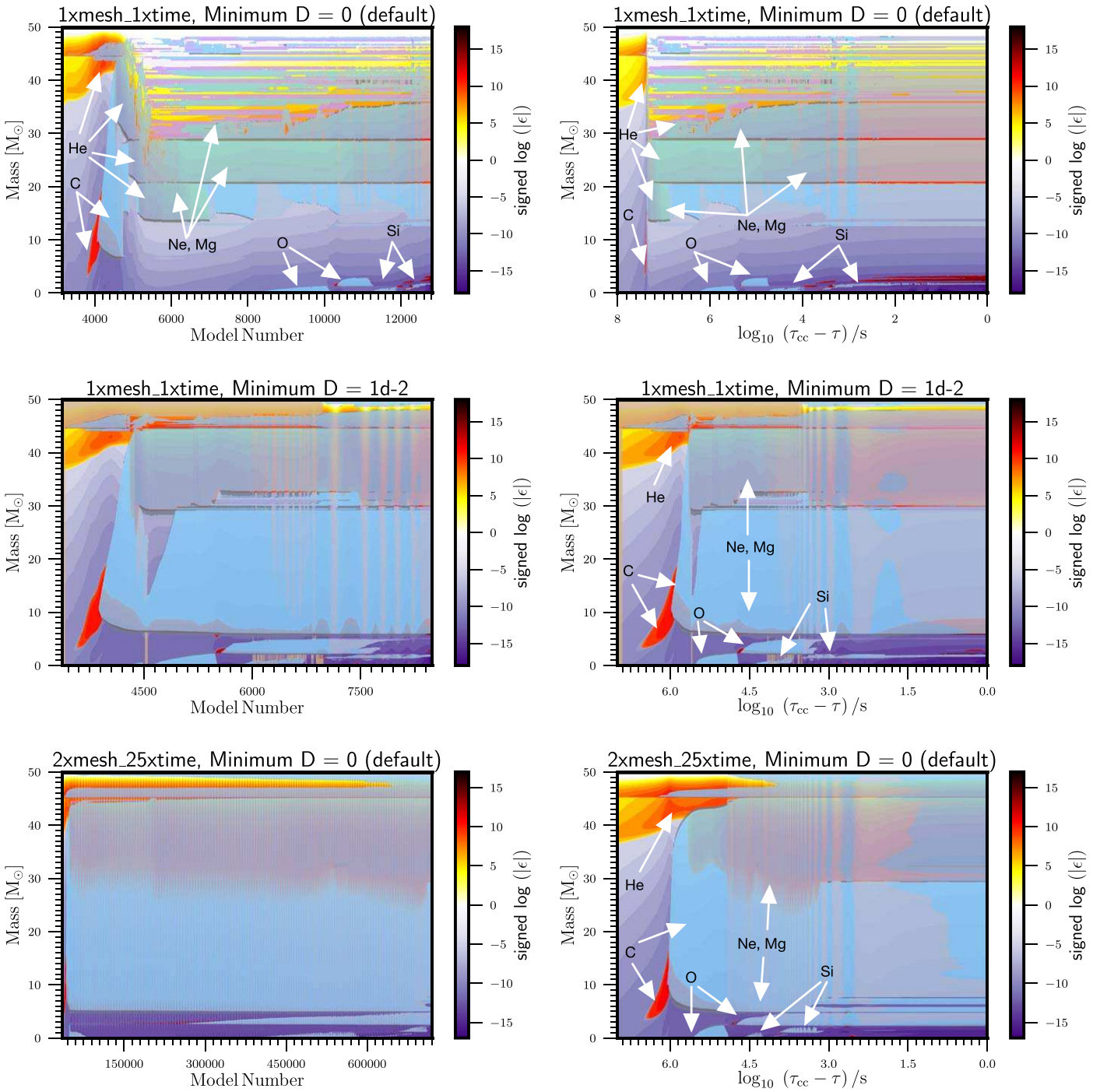

Figure 4. The difference in convection and nuclear burning between the three stellar models, as discussed in Section 3.1. The figures in the left column are shown vs. the model number from the He burning to CC. The figures in the right column are shown vs. the logarithm of the time to CC, beginning at the onset of the shell C burning. The different fuels that are burned are labeled. Each figure shows the signed logarithm of the net specific power, $\mathrm{sign}(\epsilon_{\rm nuc} - \epsilon_{\nu}) \log_{10}(\max(1.0, |\epsilon_{\rm nuc} - \epsilon_{\nu}|))$, where $\epsilon_{\rm nuc}$ is the specific energy generation rate and ϵ_{ν} is the specific energy loss from neutrinos. The purple regions denote strong neutrino cooling and the red regions denote regions of strong nuclear burning. The light blue regions indicate standard-mixing-length convection, the gray regions indicate convection with reduced mixing, because of the shorter convective timescales, and, for model 2, the beige–orange regions (e.g., near the surface) indicate where the diffusive mixing coefficient is set to $D = 10^{-2}$ cm^2 s^{-1}.

and 12,000–25,000 cells, respectively, during the hydrodynamic phase of evolution. The number of cells typically increases from the lower bound to the higher bound as a model evolves, and the average density of the model generally increases (except during pulses). Models with time steps set by `1t`, `2p5t`, `5t`, `10t`, and `25t` generally take between 8000–40,000, 15,000–150,000, 20,000–200,000, 40,000–500,000, and 100,000–1,800,000 time steps to reach CC, depending on the number of pulses encountered during the evolution. Models that produce the peak of the BH mass spectrum tend to be the most stable, and undergo less pulsational behavior than neighboring models to the left and right of the peak. At `2m_2h_25t`, models with $M_{\rm He} =$ 50–58 $M_{\odot}$ undergo many weak and some strong pulsations,

Table 1
Initial He Core Mass, Composition at He Depletion, and Resolution Controls for the Models Producing the Peak BH Mass below the Upper Mass Gap

Name	min D	max_dq	split_nz	$\delta_{\log \rho_c}$	M_{He} ($M_\odot$)	$M_{CO_{He}}$($M_\odot$)	X(^{12}C)$_{He}$	Pulses	M_{BH}($M_\odot$)
1m_1h_1t[a] (Farmer et al. 2020)	0	1d-3	6000	2.5d-3	53	47.59	0.1807	0	52.77
2m_1h_2p5t (Mehta et al. 2022)	0	5d-4	6000	1d-3	60	54.51	0.1699	1 strong, 6 weak	59.17
1m_1h_2p5t	0	1d-3	6000	2.5d-3	58	52.53	0.1730	1 strong, ∼6 weak	57.40
2m_2h_2p5t	0	5d-4	12000	2.5d-3	54	53.76	0.1757	4 strong, >50 weak	52.3
2m_2h_5t	0	5d-4	12000	5d-4	60	54.50	0.1696	1 strong, ∼7 weak	59.07
2m_2h_5t_D	1d-2	5d-4	12000	5d-4	60	54.15	0.1694	1 strong, ∼7 weak	59.23
2m_2h_25t	0	5d-4	12000	1d-4	62	56.24	0.1670	1 strong, ∼9 weak	60.61
5m_2h_2p5t	0	2d-4	30000	1d-3	55	48.92	0.1687	0	54.76
5m_5h_2p5t	0	2d-4	30000	1d-3	55	48.92	0.1687	0	54.76
5m_5h_5t	0	2d-4	30000	5d-4	57	50.34	0.1688	1 strong, ∼10 weak	53.43
5m_5h_5t_D	1d-2	2d-4	30000	5d-4	57	50.28	0.1719	1 strong, ∼5 weak	55.41
5m_2h_10t	0	2d-4	12000	2.5d-4	62	56.29	0.1672	1 strong, ∼10 weak	60.17
5m_2h_10t_D	1d-2	2d-4	12000	2.5d-4	62	56.39	0.1673	1 strong, ∼10 weak	60.07
5m_2h_25t	0	2d-4	12000	1d-4	62	56.17	0.1674	1 strong, ∼10 weak	60.55
5m_5h_25t	0	2d-4	30000	1d-4	62	56.17	0.1674	1 strong, ∼10 weak	60.32
5m_5h_25t_D	1d-2	2d-4	30000	1d-4	62	56.17	0.1674	1 strong, ∼10 weak	60.37

Note.
[a] In Farmer et al. (2020), the default values are max_dq=1d-3, split_merge_amr_nz_baseline = 6000, and delta_lgRho_cntr_limit = 2.5d-3. All models in this table are scaled multiples of these values. For example, 2m_2h_2p5t represents two times the number of cells during the hydrostatic phase, two times the number of cells during the hydrostatic and hydrodynamic phases, and 2.5 times the temporal resolution during all phases of evolution. split_merge_amr_nz_baseline is labeled as split_nz, and delta_lgRho_cntr_limit is labeled as $\delta_{\log \rho_c}$. M_{CO_He} and X(^{12}C)$_{He}$ are the C–O core mass and the central ^{12}C mass fraction at core He depletion, respectively.

reducing the BH mass and deviating from linear growth in the BH mass. $M_{He} = 60$–$62\,M_\odot$ models are the most stable, resulting in few pulsations, and at $M_{He} \geqslant 63\,M_\odot$ strong pulses mixed with weak pulses result in much less massive BH masses.

All models were run on eight-core nodes and allotted 32 GB of RAM. The wall-clock times are generally between one and four days for low-resolution models (e.g., 1m_1h_1t–2m_2h_5t), one to three weeks for intermediate-resolution models (e.g., 5m_5h_2p5t–5m_2h_10t), and one to 10 weeks for the highest-resolution models (e.g., 2m_2h_25t). The highest-resolution models take between one to three weeks near the BH mass spectrum peak, between three to 10 weeks to the left of the peak, where hundreds of weak pulsations occur, and between three to 10 weeks to the right of the peak, where strong pulsations are intermixed with weak pulsation episodes. The computational cost of 2m_2h_25t prevented us from computing full spectra at higher-mass resolutions, such as 5m_5h_25t. In this work, these models could not feasibly be calculated anywhere other than at the BH spectrum peak, as they would take between three and nine months to complete. Models that did not reach CC or did not result in a PISNe are not included in this work.

In Table 1, all models except 1m_1h_t possess central X(^{12}C)$_{He}$ mass fractions within 0.01 of each other at core He depletion, regardless of the initial He core mass M_{He}. The C–O core mass M_{CO_He} at He depletion primarily depends on M_{He}. Models with similar initial M_{He} develop values of M_{CO_He} within $1\,M_\odot$ of each other, regardless of the adopted resolution. Our CO and He core mass boundaries are defined as the outermost locations where X(^{4}He) $\leqslant 0.01$ and X(^{1}H) $\leqslant 0.01$, respectively.

Across all resolutions, the behaviors of each PPISN model shown in Figure 5 are similar. Regardless of the He core mass, each model undergoes He core burning followed by shell He burning, as the core beneath contracts. In all cases, the contracting core is momentarily stabilized by the central C ignition radiatively burning outward, and leaving behind an O–Mg-rich core, with traces of Si. The next evolutionary phase is primarily determined by the total mass of the C–O core at the end of the He burning, which scales linearly with M_{He}, and the X(^{12}C) of the shell that is identical to X(^{12}C)$_{He}$, the X(^{12}C) mass fraction at He depletion. If the core is not massive enough, or X(^{12}C)$_{He}$ is large enough, a convectively burning carbon shell will form and the core will undergo stable convective O ignition, to maintain hydrostatic equilibrium. This sort of evolution is characterized by a smooth transition from C to O/Ne/Mg, and then to Si/S/Ar, and eventually to Fe burning in the core. This leads the star to CC without any dynamical contractions or pulses driven by Γ_1 instability. These stellar models only lose mass through winds during He burning, $M_{eject} \leqslant 0.3\,M_\odot$, and thus produce linear growth in the BH spectrum, in correspondence with the initial He core mass. For $\sigma[^{12}\mathrm{C}(\alpha,\gamma)^{16}\mathrm{O}] = 0$, the left side of the BH mass spectrum is stable up to $M_{He} \simeq 47\,M_\odot$, at which point the lower edge of the pulsational pair-instability strip is encountered. Models that are slightly more massive than $M_{He} \simeq 47\,M_\odot$, and/or with slightly lower X(^{12}C)$_{He}$, begin to suffer from pair instability in their interiors, fueling a dynamic evolution toward CC. Just above $M_{He} \simeq 47\,M_\odot$, the pair production in the interiors of these stellar cores softens the equation of state, and dynamical contractions begin to drive weak pulses that remove material from the surfaces of these models. As M_{He} increases, the weak pulses increase in frequency and number, until strong pulses develop, unbinding $M_{eject} \geqslant 1\,M_\odot$ until the peak of the BH mass spectrum is encountered. More details of the characteristics of the weak pulsations that are encountered before the peak are discussed in Woosley (2017) and Renzo et al. (2020a), although not at the highest resolutions explored in this work. Weak pulsations begin to develop when convective shell C burning cannot supply the energy needed to stabilize the shell long enough for smooth O ignition in the center. The onset of

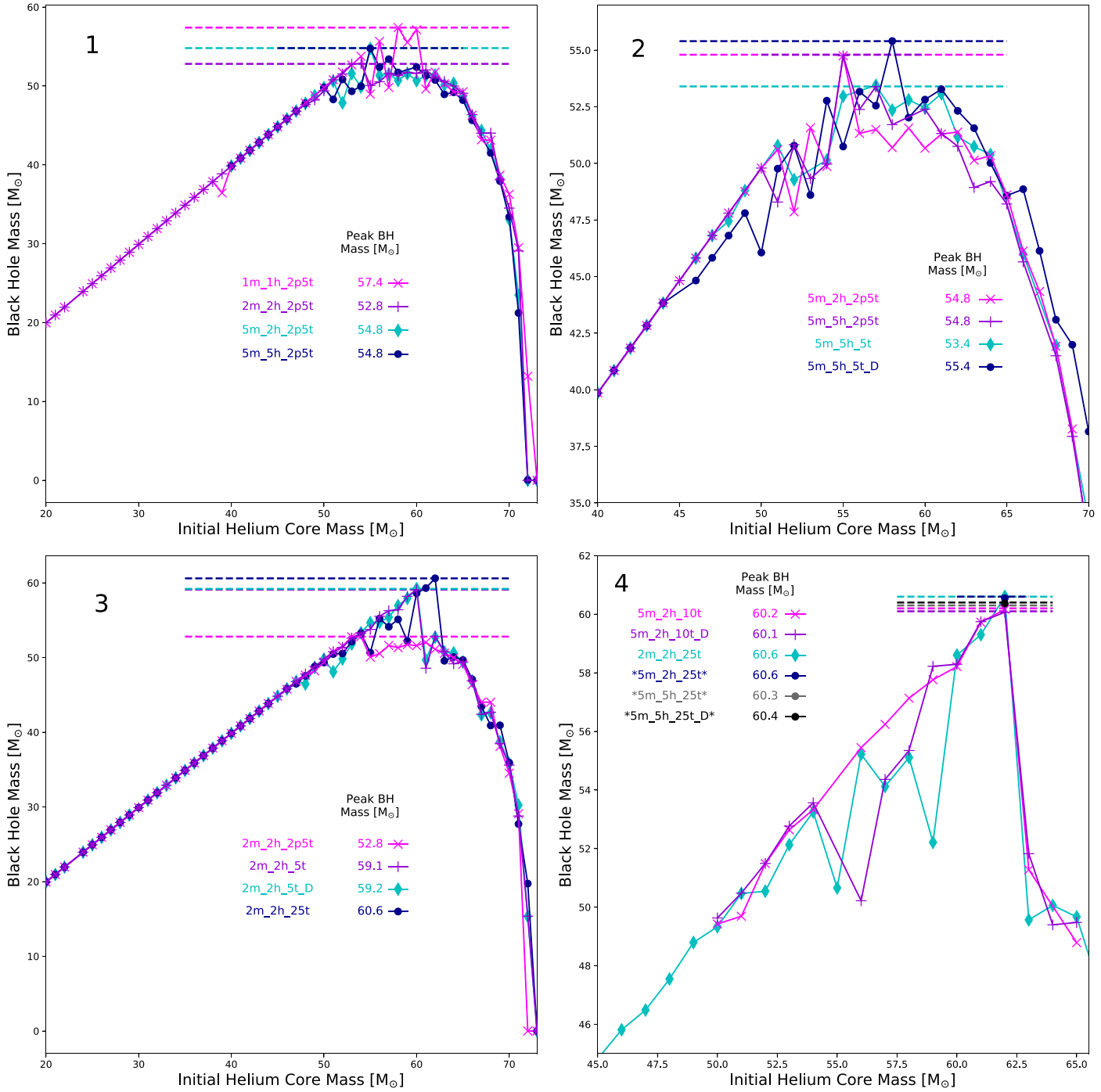

Figure 5. BH mass spectra for the resolutions in Table 1. All panels share a similar x-axis, the initial He core mass $M_{\rm He}$ in $M_\odot$, and y-axis, the BH mass in $M_\odot$. Resolutions that are only shown at their respective peak BH masses are labeled with asterisks on either side. The horizontal dashed and solid lines indicate the location of the peak BH mass for each resolution.

this instability is discussed in detail in the behavior of the 50 $M_\odot$ He cores in Section 3.1. Stronger pulsations near to and at the peak of the BH mass spectrum typically involve a short episode of convective shell C burning, while a portion of the central O core convectively burns. Once ^{12}C is nearly depleted from the shell, Γ_1 instability leads to a dynamical contraction, followed by a thermonuclear explosion of a significant mass fraction of the O-rich core. When the shock reaches the surface of the model, multiple contractions and bounces occur, as the star relaxes back to hydrostatic equilibrium. After a dynamical episode, stable O burning can ensue in the core, followed by the burning of heavier isotopes, and eventually CC.

To the right of the BH mass spectrum peak, all models with larger $M_{\rm He}$ are unable to develop sufficient pressure from shell C burning to enable smooth O ignition in the core. The convective growth of the C-burning shell is undercut by a Γ_1 instability, resulting in an infalling core that radiatively burns through most of its neon on a timescale of $\lesssim$50–70 s, followed by explosive burning of the central O core in the next $\lesssim$50 s. Nearly all of the central ^{16}O is burned in this explosive burning

episode, removing between ≃5 and 30 $M_\odot$ of material after just one strong pulse and the weak pulses that follow. These pulses are so strong that they temporarily perturb the model for 1–10^3 yr. After the model relaxes back into hydrostatic equilibrium, nuclear burning recommences, and one or several more strong and weak pulsing episodes may follow, depending on the strength of the initial pulse and the amount of unburned ^{16}O remaining in the core. For models with $M_{\rm He} \geqslant 72\,M_\odot$, the O-rich core explodes in a single thermonuclear pulse, driving a supersonic shock with energy greater than the total binding energy of the model, disrupting the entire model after a single pulse, and leaving no compact remnant in a PISNe.

In panel 1 of Figure 5, we compare the BH mass spectrum at three resolutions with increasing mass resolution and otherwise equal temporal resolution. Models with $M_{\rm He} \leqslant 47\,M_\odot$ do not appear to encounter pulsational pair instability, according to panel 1, as this appears to be the lower edge of the pair-instability strip. The first resolution to display PPISN behavior is `5m_5h_2p5t`, followed by `5m_2h_2p5t`, `2m_2h_2p5t`, and then `1m_1h_2p5t`. Increasing the mass resolution appears to smooth out the peak of the BH mass spectra, although this could be due to a lack of temporal resolution to accurately resolve models with greater mass resolution. The erratic behavior near the peak for `1m_1h_2p5t` is likely due to it being slightly underresolved. Convergence in the peak BH mass is observed between `5m_5h_2p5t` and `5m_2h_2p5t`. Both resolutions predict a BH mass peak of $M_{\rm BH} \simeq 54.8\,M_\odot$, satisfying our criteria for convergence at the $<1\,M_\odot$ level. This convergence is slightly suspect, though, as both models evolved from a $55\,M_\odot$ He core that did not enter the hydrodynamic solver during the core O burning, remaining in the implicit hydrostatic solver until the HLLC hydrodynamic solver was turned on at CC; refer to Marchant et al. (2019) for a discussion of the criterion for turning on the HLLC solver. Directly to the right of the peak, all the model resolutions appear to fall within 1–2 $M_\odot$ of one another.

In panel 2 of Figure 5, we compare our previously converged mass resolution models with two additional resolutions at twice the temporal resolution, with and without a minimum diffusive mixing floor, `5m_5h_5t` and `5m_5h_5t_D`. This comparison illustrates that while the mass resolution might be converged, increasing the temporal resolution and including a minimum diffusive mixing floor changes the peak BH mass at the $>1\,M_\odot$ level, indicating that our models are not fully time-resolved near the peak. There is a wide spread in BH mass across the entire peak, another indication that increasing the temporal resolution of these models might be warranted.

In panel 3, we conduct a test of the temporal resolution of these models by controlling for changes in the central density per time step. Increasing from `2m_2h_2p5t` to `2m_2h_25t`, an order of magnitude increase in the temporal resolution, leads to a change in the BH mass of ≃8 $M_\odot$. This is a significant increase in the peak BH mass, demonstrating the importance of time resolution in resolving the convective burning behavior of our PPISN models. To the left of the peak, the number of weak pulses resolved is also particularly sensitive to time resolution. This is one of the primary reasons that `2m_2h_25t` takes >1,000,000 time steps in models between 50 and 58 $M_\odot$. These models are able to resolve hundreds of weak pulses, creating small shocks that unbind between 0.5 and 1 $M_\odot$ of material. In several cases (e.g., $M_{\rm He} = 53$, 54, 55, and 59 $M_\odot$), these weak shocks precede the development of an episode of strong shocks that can go entirely unresolved at resolutions lower than `2m_2h_25t`, straying from the trend of the linear growth in $M_{\rm BH}$ observed at lower resolutions. Hundreds of weak shocks are also observed to the right side of the BH mass spectrum peak. Between each strong shock, hundreds of weak shocks can remove multiple $M_\odot$ of additional material.

In panel 4, we show the resolved peak of the BH spectrum from our highest-temporal resolution models and confirm its existence at our highest adopted mass resolution. By comparing our highest temporal resolution, `2m_2h_25t`, with `5m_2h_10t` and `5m_2h_10t_D`, we confirm that 10 times the temporal resolution is needed to resolve the BH mass spectrum peak to within $\leqslant 1\,M_\odot$. We confirm the convergence of these models by including the peak BH masses from `5m_2h_25t`, `5m_5h_25t`, and `5m_5h_25t_D`. In conjunction with Table 1, panel 4 illustrates that the adoption of a minimum diffusion coefficient $D_{\rm min}$ changes the peak BH mass at the $\leqslant 0.1\,M_\odot$ level. Models with $D_{\rm min}$ also tend to be more numerically stable than models run without, encountering fewer overall crashes, and typically achieving their final fate in fewer time steps and, therefore, in a generally lower wall-clock time, even for similar BH masses.

Looking at all four panels, we are able to differentiate between the importance of the mass and temporal resolutions. The amount of mass resolution needed to resolve the peak is limited by the amount of temporal resolution available. For example, models run with `2m_2h_5t` are more stable than models run with `5m_5h_5t`, displaying respective peak BH masses of $M_{\rm BH} \simeq 59.1\,M_\odot$ and $M_{\rm BH} \simeq 53.4\,M_\odot$. We find that an adequate amount of temporal resolution is necessary to resolve the peak at a given mass resolution. Models with large mass and low time resolutions tend to produce the most smeared peaks, with the lowest overall peak BH masses, whereas models with low mass resolution and high temporal resolution display the largest overall peak BH masses. This explains why `1m_1h_2p5t` is able to resolve a larger peak BH mass than at any other mass resolution, with a similar time resolution. Increasing the mass resolution in a vacuum is not advised, without comparable increases in temporal resolution. Panel 4 indicates that time steps that are limited by at least $\delta_{\log \rho_c} \leqslant 2.5 \times 10^{-4}$ are needed to resolve the peak BH mass, and that $\delta_{\log \rho_c} \leqslant 10^{-4}$ is needed to accurately resolve the shape of the BH mass spectrum, while the amount of mass resolution needed is rather unclear.

Marchant & Moriya (2020) and Woosley & Heger (2021) found that the efficiency of the angular momentum transport changes the lower edge of the BH's mass gap at the ≃10% level. Farmer et al. (2019) found that the lower edge of the mass gap was robust at the ≃10% level to changes in the metallicity, the wind mass-loss prescription, and the treatment of chemical mixing. In Renzo et al. (2020c), for the convection during pulses, we showed that the treatment of time-dependent convection does not directly affect the maximum BH mass. In Mehta et al. (2022), we claimed that our models for the peak BH mass were robust with respect to mass and temporal resolutions at the ≃10% level. In this section, we have gone further and shown that by adopting a resolution of `5m_2h_10t` or `5m_2h_10t_D`, our peak BH mass models are robust to mass and temporal resolution at the ≃1% level at $\sigma[^{12}{\rm C}(\alpha,\gamma)^{16}{\rm O}] = 0$.

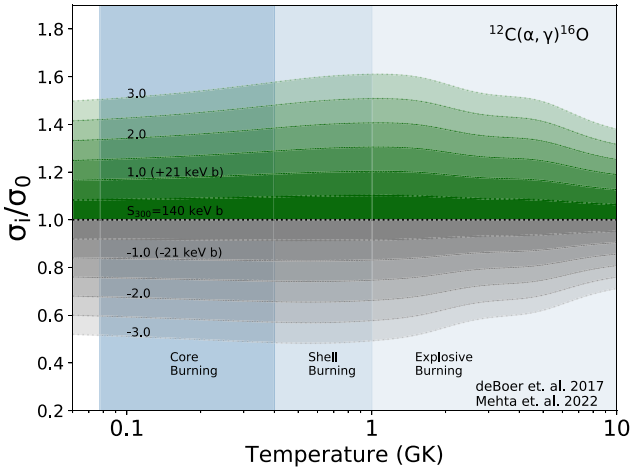

Figure 6. ^{12}C(α, γ) reaction rate ratios, σ_i/σ_0, as a function of temperature. σ_i spans −3.0 to 3.0 in 0.5 step increments, with σ_0 being the current nominal rate. Negative σ_i are shown with the gray curves and positive σ_i are shown with the green curves. The ±1, 2, and 3 σ_i curves are labeled. The blue band shows the range of temperatures encountered during the core and shell He burning.

4. The Rate-dependent Single-star BH Mass Gap

During the core He burning phase of stellar evolution, a competition between the (3α) process ^{4}He (α,)^8 Be (α,)^{12} C *(, 2γ)^{12}C and ^{12}C(α,γ)^{16}O establishes the C/O ratio of the stellar core for the later C- and O-burning phases. The evolution of the He cores through the advanced burning stages depends sensitively on the C/O ratio of these models at He depletion. Reducing the uncertainty in the ^{12}C(α,γ)^{16}O reaction rate probability distribution function is a goal of forthcoming experiments (deBoer et al. 2017; Smith et al. 2021). A common approach to investigating the C/O ratio of differing stellar cores is to explore a modified ^{12}C(α,γ)^{16}O during He burning and to trace its effect on the BH mass distribution (Takahashi 2018; Farmer et al. 2020; Costa et al. 2021; Mehta et al. 2022). In this section, we will continue with a similar exploration of this rate, albeit at a significantly higher model resolution than similar works that have previously been conducted in MESA. We will explore variations in ^{12}C(α,γ)^{16}O at the 0.5σ level, with the ^{12}C(α,γ)^{16}O rate provided by deBoer et al. (2017) and updated in Mehta et al. (2022); see Figure 6. σ_o represents the median rate consistent with an astrophysical S-factor of S(300 keV) = 140 keV b, with a ±1 σ = 21 keV b uncertainty. By exploring ±3σ, we effectively explore the range S(300 keV) = (77,203) keV b, where positive and negative σ indicate stronger and weaker rates than the median value, respectively.

In this section, we will explore a range of MESA stellar model resolutions across the rate-dependent upper mass gap. In Section 4.1, we extend our resolution study to resolve the tip of the BH mass spectrum at the $\leqslant 2\,M_\odot$ level, at $\sigma[^{12}\mathrm{C}(\alpha,\gamma)^{16}\mathrm{O}] = -3, +3$, and we recompute a newly resolved lower edge to the BH mass gap. In Section 4.2, we discuss the impact of a newly calculated ^{4}He (2α,)^{12}C (3α) reaction rate on the location of the lower edge of the ^{12}C(α,γ)^{16}O rate-dependent mass gap. We then recompute a resolved lower edge to the rate-dependent mass gap with the inclusion of this revised 3α rate. We end this section by comparing our new lower BH mass gap edge with recent measurements of BBH mergers detected in the third Gravitational-Wave Transient Catalog (GWTC-3) by The LIGO Scientific Collaboration et al. (2021).

4.1. Resolving the $^{12}C(\alpha,\gamma)^{16}O$-dependent BH Mass Gap

By varying the ^{12}C(α,γ)^{16}O rate, we probe the convergence of models with differing C/O cores. We then establish a new resolved lower edge of the upper mass gap as $M_{\rm lower} \simeq 60^{+32}_{-14}$ $M_\odot$, from the ±3σ uncertainty in ^{12}C(α, γ)^{16}O. In Figure 7, we compute the BH mass spectra and their associated peak BH masses at five different resolutions found in Table 1. In each panel, we display the BH mass spectra produced by adopting the model resolutions found in Farmer et al. (2020; `1m_1h_1t`) and Mehta et al. (2022; `2m_1h_2p5t`), our highest feasible temporal resolution, `2m_2h_25t`, and `5m_2h_10t_D`, which we have shown to reproduce the BH mass spectrum peak to within $\leqslant 1\,M_\odot$ at $\sigma[^{12}\mathrm{C}(\alpha,\gamma)^{16}\mathrm{O}] = 0$. We opt only to compute BH mass spectra across the peak for `5m_2h_10t_D`, as these models tend to be much more numerically stable than models run with `5m_2h_10t`, encountering fewer overall crashes than models that do not adopt $D_{\rm min}$. In each panel, only the peak BH mass is shown for `5m_2h_10t`, to illustrate the similar agreement with `5m_2h_10t_D`.

In the top panel of Figure 7, we show the BH mass spectra for models with $\sigma[^{12}\mathrm{C}(\alpha,\gamma)^{16}\mathrm{O}] = -3$. These models possess larger C/O mass fractions, with typical X(^{12}C)∼0.32. The larger ^{12}C mass fractions of these He cores allow for the development of strong convective shell C burning, which manages to counter the effects of pair instability in these cores long enough for them to reach CC (Takahashi 2018; Woosley & Heger 2021). There is little shape to these spectra, as the models are stable until they explode as PISNe. If the true cosmic ^{12}C(α,γ)^{16}O rate was in fact this weak, we would not expect to observe any PPISN stars, as the lower edge of the pair-instability strip is synchronous with the lower edge of the BH mass gap. Here, Farmer et al. (2020; `1m_1h_1t`), Mehta et al. (2022; `2m_1h_2p5t`), and `2m_2h_25t` produce BHs of identical mass, $M_{\rm BH} \simeq 93.4\,M_\odot$. The models `5m_2h_10t` and `5m_2h_10t_D` appear to agree with one another, producing BHs with identical mass $M_{\rm BH} \simeq 91.4\,M_\odot$. Interestingly, our lowest-resolution model illustrates better agreement with our highest-resolution model than our moderate-resolution models. As a check, we have computed an additional model with `5m_2h_25t` and found that the peak BH mass remains $M_{\rm BH} \simeq 93.4\,M_\odot$. It is unclear why our lowest-resolution models agree with our highest-resolution models here; however, in a stellar evolution model, there are many choices that are made that interact in highly nonlinear ways with one another. It is possible that our experiment, which varies only a few parameters, does not capture all of the possible variations necessary. Nonetheless, the location of the BH mass spectrum peak is sensitive to temporal resolution, due to its discontinuous nature. In this case, we are able to resolve the peak BH mass spectrum at lower resolutions, but we can only be confident in our peak BH mass estimate to within $\leqslant 2\,M_\odot$ with `5m_2h_10t_D`.

In the middle panel of Figure 7, we show the BH mass spectra for models with $\sigma[^{12}\mathrm{C}(\alpha,\gamma)^{16}\mathrm{O}] = 0$. The behaviors of models with these C/O mass fractions, X(^{12}C)∼0.17, were previously discussed in Section 3.2. Within the context of our MESA models, Mehta et al. (2022) has shown the dependence of the BH mass spectrum on the tabulated temperature

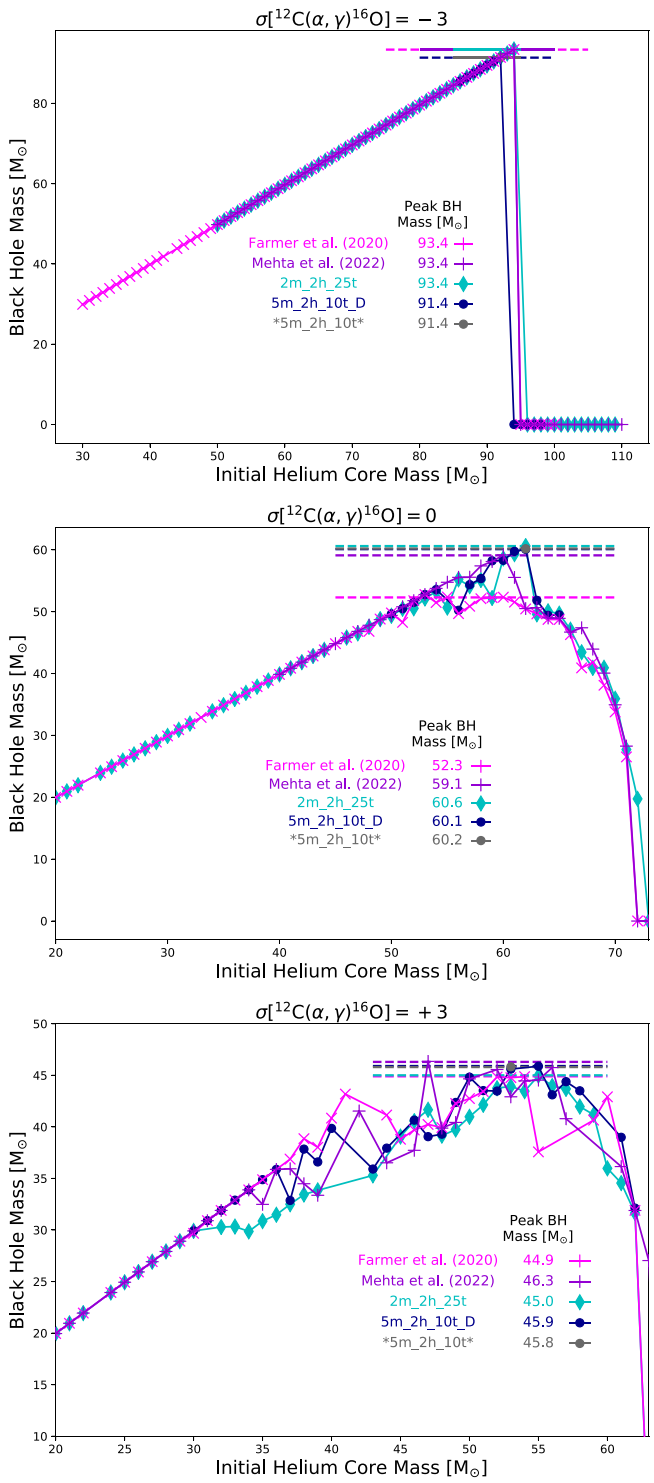

Figure 7. The BH mass spectra for different values of the $^{12}C(\alpha,\gamma)^{16}O$ rate—top ($\sigma = -3$); bottom ($\sigma = +3$); and middle ($\sigma = 0$)—for five of the resolutions listed in Table 1. All panels share a similar x-axis, the initial He core mass M_{He} in $M_\odot$, and y-axis, the BH mass in $M_\odot$. Resolutions that are only shown at their respective peak BH masses are labeled with asterisks on either side. The horizontal dashed and solid lines indicate the location of the peak BH mass for each resolution.

resolution of the $\sigma = 0$ $^{12}C(\alpha,\gamma)^{16}O$ reaction rate at `2m_1h_2p5t`. When the reaction rate was defined by 52 temperature points, the BH mass spectrum reached a maximum BH mass of 49.6 $M_\odot$ at an initial He core mass of 55.0 $M_\odot$. When the reaction rate was defined by 2015 temperature points, the BH mass spectrum reached a maximum BH mass of 59.1 $M_\odot$ at an initial He core mass of 60.0 $M_\odot$. In this work, we have confirmed the maximum BH mass to be 60.3–60.4 $M_\odot$, with an initial He core mass of 62 $M_\odot$ at our highest resolution, `5m_5h_25t`. Mehta et al. (2022) happened to choose a combination of mass and temporal resolution that was able to resolve the peak of the BH mass to within 2 $M_\odot$ of the resolved value. As a result, the ability of the 2015 point rate to produce models that sustain a linear trend of larger BH masses with larger initial He core masses was not just a result of the improved tabulated resolution of the $^{12}C(\alpha,\gamma)^{16}O$ reaction rate, but also largely due to the resolution of the models used to calculate the peak in Mehta et al. (2022). In this work, the peak of the $\sigma[^{12}C(\alpha,\gamma)^{16}O] = 0$ BH mass spectrum can only be resolved to within $\leqslant 1\,M_\odot$ with `5m_2h_10t_D` or greater resolutions.

In the bottom panel of Figure 7, we show the BH spectra for models with $\sigma[^{12}C(\alpha,\gamma)^{16}O] = +3$. These models possess the lowest overall C/O mass fractions, with typical $X(^{12}C) \sim 0.07$. Given the small C/O mass fractions present in these cores, most of these models undergo at least one strong pulse. At the lower end of the BH mass spectra, a notable difference in the location of the lower edge of the pair-instability strip can be seen between `2m_2h_25t` and all other resolutions. From this panel, we find that the lower edge of the pair-instability strip is $\simeq 32\,M_\odot$ at `2m_2h_25t`, $\simeq 5\,M_\odot$ lower than at any other resolution. Temporal resolution appears to be of critical importance in establishing the lower edge of the pair-instability strip for models with low C/O mass fractions. Models with low temporal resolution are unable to resolve the hundreds of weak pulses that culminate in a strong pulse for models with M_{He} as low as 32 $M_\odot$. Across the mass spectra, a large spread in the BH masses is found at varying resolutions, with the primary difference being owed to the sheer number of weak pulsation episodes intermixed between the strong pulses. The models run at `2m_2h_25t` are able to resolve many more weak pulses than at any other resolution, leading to BH masses that are typically lower than those predicted by lower resolutions. At $\sigma[^{12}C(\alpha,\gamma)^{16}O] = +3$, we are able to resolve the peak BH mass to within $\leqslant 1\,M_\odot$, with `5m_2h_10t_D`, although we cannot resolve the entire shape of the BH mass spectrum.

Figure 7 shows that the temporal resolution during the hydrodynamic phase of evolution is most important for resolving the peak of the BH mass spectrum. This is due to the tight coupling between the nuclear burning and convection at each time step. Models with $\sigma[^{12}C(\alpha,\gamma)^{16}O] = -3$ spend the least amount of time in the hydrodynamic phase, while models with $\sigma[^{12}C(\alpha,\gamma)^{16}O] = +3$ spend the most. The BH mass spread between different temporal resolutions is larger the longer that these models spend in the hydrodynamic phase. Models with stronger $^{12}C(\alpha,\gamma)^{16}O$ rates undergo stronger nuclear burning episodes and convection, requiring the highest temporal resolutions to resolve.

Given the large computational cost of computing models with `2m_2h_25t`, we adopt `5m_2h_10t_D` as our highest resolution moving forward, with numerical convergence in the peak BH mass at the $\leqslant(2,\ 1,\ 1)M_\odot$ level for $\sigma[^{12}C(\alpha,\gamma)^{16}O] = -3,\ 0,\ +3$. More specifically, the models run with `5m_2h_10t_D` appear to underestimate the peak BH mass by $\leqslant 2\,M_\odot$ at $\sigma = -3$ and to overestimate the peak BH mass by $\leqslant 1\,M_\odot$ at $\sigma = 3$. In Figure 8, we compute the lower

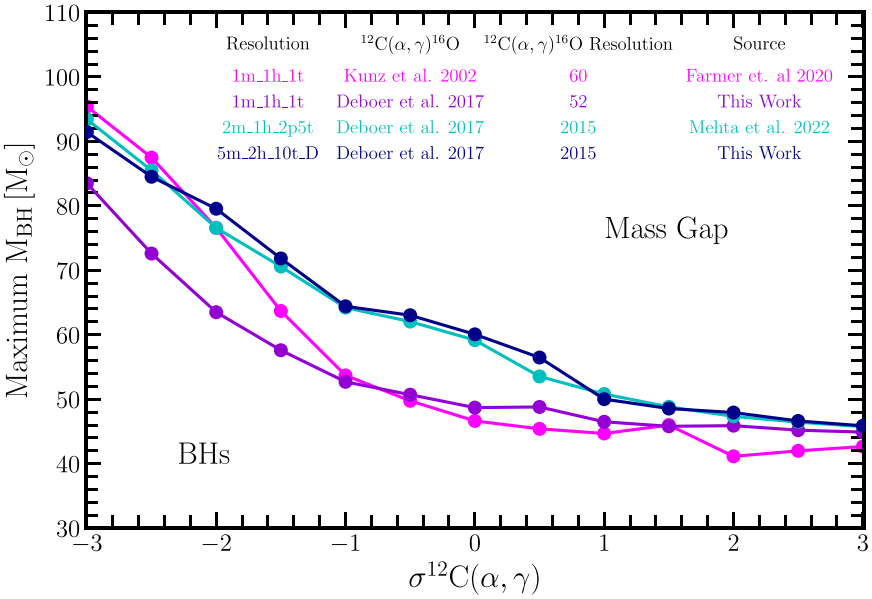

Figure 8. The location of the lower edge of the BH mass gap as a function of the temperature-dependent uncertainty in the $^{12}C(\alpha,\gamma)^{16}O$ reaction rate. The lines mark the lower mass gap boundaries predicted by the adopted $^{12}C(\alpha,\gamma)^{16}O$ rate uncertainties. The pink line marks the lower mass gap boundary as found in Figure 5 of Farmer et al. (2020), predicted by the Kunz et al. (2002) rate as expressed in the STARLIB reaction rate library (Sallaska et al. 2013). The dark purple line marks the lower mass gap boundary predicted by models adopting the resolution from Farmer et al. (2020) and the original 52–temperature point $^{12}C(\alpha,\gamma)^{16}O$ rate provided by deBoer et al. (2017). The coral blue line marks the lower mass gap boundary using the updated $^{12}C(\alpha,\gamma)^{16}O$ calculated and implemented in Mehta et al. (2022). The dark blue line marks the revised lower mass gap boundary calculated in this work using the updated $^{12}C(\alpha,\gamma)^{16}O$ adopted in Mehta et al. (2022). Note that $\sigma[^{12}C(\alpha,\gamma)^{16}O]$ represent different astrophysical S-factors for each rate source.

edge of a resolved $^{12}C(\alpha,\gamma)^{16}O$ rate-dependent BH mass gap and compare to previous work. In Farmer et al. (2020), using a default resolution of 1m_1h_1t, a 60–temperature point $^{12}C(\alpha,\gamma)^{16}O$ from STARLIB (Kunz et al. 2002) was calculated and discussed, along with the deBoer et al. (2017) $^{12}C(\alpha,\gamma)^{16}O$ rate at $\sigma=-1$, 0, 1. In this work, we extend that calculation across the lower edge of the mass gap, to show the result of adopting the original 52–temperature point deBoer et al. (2017) $^{12}C(\alpha,\gamma)^{16}O$ rate at 1m_1h_1t. While the agreement between deBoer et al. (2017) and Kunz et al. (2002) was $\leqslant 3\,M_\odot$ at $\sigma=-1$, 0, 1, the difference between both rates grows appreciably large between $\sigma=-1$, -3. This is due to the fact that σ does not represent the same physical quantity, the astrophysical S-factor, for different sources of the reaction rate.

In Mehta et al. (2022), a revised deBoer et al. (2017) reaction rate probability distribution function defined by 2015 temperature points at each σ_i was adopted and implemented at an improved resolution of 2m_1h_2p5t. This small improvement to the model and reaction rate resolution substantially increased the lower edge of the BH mass gap between $\sigma=-2$, $+3$. The resolved lower edge computed with 5m_2h_10t shows reasonable agreement with the results of Mehta et al. (2022) at the $\leqslant 4\,M_\odot$ level across the lower edge of the BH mass gap.

4.2. The Impact of 3α on the BH Mass Gap and GWTC-3

The 3α process is primarily carried out by the fusion of three α particles to form ^{12}C in the Hoyle state (Hoyle 1954), a resonant 0^+ second excited state of ^{12}C at ~7.65 Mev, which then decays into the ground state. The currently adopted rate for 3α in many stellar evolution codes comes from Nomoto et al. (1985), who adopted $\Gamma_{\rm rad}=3.7$ meV (i.e., 3.7×10^{-3} ev) as the radiative branching ratio width of the Hoyle state. All three 3α rates available for use in MESA adopt this value of $\Gamma_{\rm rad}$ in their calculations: CF88 (Caughlan & Fowler 1988), NACRE (Angulo et al. 1999), and JINA REACLIB (Cyburt et al. 2010). Up to this point, we have adopted the NACRE formulation for the 3α rate, although it should be noted that the CF88 and JINA rates are always smaller than the NACRE rate at He burning temperatures (0.2–0.4 GK); see Figure 10 in the Appendix. More recently, Freer & Fynbo (2014) have performed an up-to-date review of the relevant literature to affirm the recommended value as $\Gamma_{\rm rad}=3.7$ meV. Recent measurements by Eriksen et al. (2020), Kibedi et al. (2020), and Cook et al. (2021) have proposed a revised width of $\Gamma_{\rm rad}=5.1(6)$ meV. If true, this would imply an upward revision in the 3α rate at the 37.8% level. An increase of this magnitude would warrant a large revision to the BH mass gap, and could improve the overall agreement between recent GW detections of BBHs and the theorized existence of pair-instability stars. In Rolfs & Rodney (1988), the 3α reaction rate is quoted as being known to a 15% accuracy, and to a 10% accuracy in West et al. (2013) and Austin et al. (2014).

We explore the impact of the 3α reaction rate by implementing a 37.8% larger rate as a multiplicative factor on the currently adopted NACRE rate. Here, the NACRE rate is represented by $f_{3\alpha}=1$, while the revised rate denoted by $f_{3\alpha}=1.378$. Figure 9 shows the location of the lower edge of the $^{12}C(\alpha,\gamma)^{16}O$ rate-dependent BH mass gap at a resolution of 5m_2h_10t_D for $f_{3\alpha}=(1,\ 1.378)$, supplemented with the data provided in Table 2. Figure 9 also shows all the BHs with $M\geqslant 45\,M_\odot$ in GWTC-3 (The LIGO Scientific Collaboration et al. 2021). Testing at a resolution of 5m_2h_25t for $\sigma=-3$ confirms that the peak BH mass of $M_{\rm BH}=103.3\,M_\odot$ for $f_{3\alpha}=1.378$ remains within $\leqslant 2\,M_\odot$ of $M_{\rm BH}=105.3\,M_\odot$, the value found by the models calculated with 5m_2h_25t. The BH mass gaps shown in Figure 9 are likely to be numerically resolved with $\lesssim 2\,M_\odot$, as compared to the models run at our highest temporal resolution. At $\sigma[^{12}C(\alpha,\gamma)^{16}O]=-3$, 0, $+3$, using $f_{3\alpha}=1.378$ results in an increase in the lower edge of the

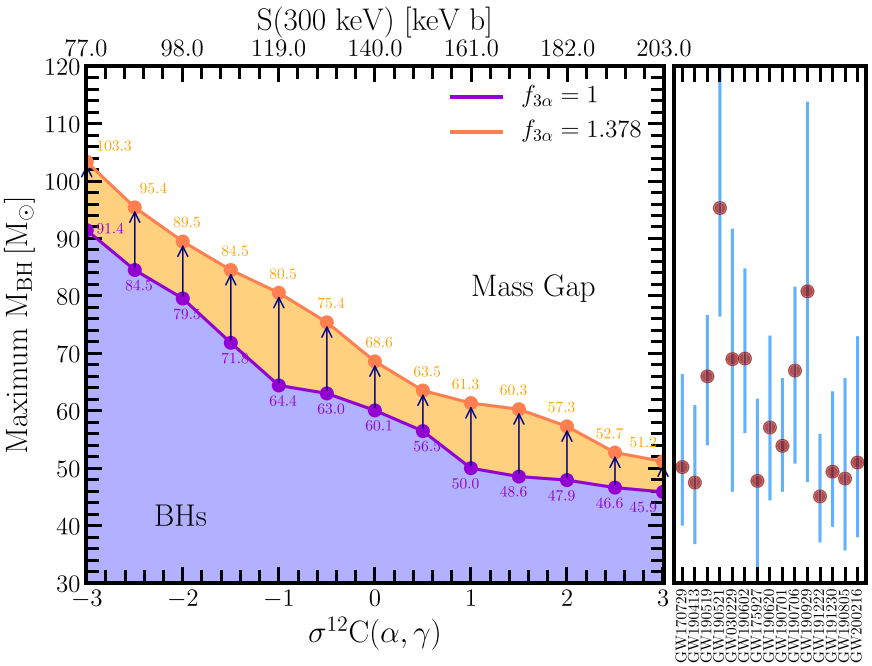

Figure 9. The location of the lower edge of the BH mass gap as a function of the temperature-dependent uncertainty in the $^{12}C(\alpha,\gamma)^{16}O$ reaction rate. The dark purple line marks the revised lower mass gap boundary calculated in this work using the updated $^{12}C(\alpha,\gamma)^{16}O$ adopted in Mehta et al. (2022) and $f_{3\alpha} = 1$ (Angulo et al. 1999). The orange line marks the revised lower mass gap boundary calculated in this work using the updated $^{12}C(\alpha,\gamma)^{16}O$ adopted in Mehta et al. (2022) and $f_{3\alpha} = 1.378$ (Kibedi et al. 2020). The white region denotes the mass gap and the yellow–orange regions highlight the differences between the models computed with $f_{3\alpha} = 1$ and $f_{3\alpha} = 1.378$ with the same uncertainty in $^{12}C(\alpha,\gamma)^{16}O$. All the BH masses with $M_{BH} \geqslant 45\,M_\odot$ included in GWTC-3 are shown with the dark red points, with the blue error bars showing the uncertainty in their inferred mass. The approximate astrophysical S-factor corresponding to each probability distribution function–sourced σ value is labeled on the top of the x-axis.

upper stellar mass gap of $M_{BH} = (11.9,\ 8.4,\ 5.3)M_\odot$, respectively, yielding $M_{lower} \simeq 69^{+34}_{-18}$ /Msun.

In rotating stars, the pulsational instability region is shifted by the additional centrifugal force. This causes the BH masses to increase, depending on the efficiency of the angular momentum transport. Marchant & Moriya (2020) showed that under assumptions that maximize the impact of rotation on the gap (no angular momentum transport and fast rigid rotation at He ignition), the shift in the peak BH mass is $\lesssim 10\%$, similar to the findings of Woosley & Heger (2021).

Assuming that GW190521 formed as an isolated $M = 95.3\,M_\odot$ BH implies an S-factor of $\gtrsim$77 keV b (or 88 keV b with an enhanced 3α rate). This is consistent with the 73^{+11} keV b inferred by Farmer et al. (2020), which used the Kunz et al. (2002) $^{12}C(\alpha,\gamma)^{16}O$ reaction rate. The next most massive BH, GW190929, with $M = 80.8\,M_\odot$, implies an S-factor $\gtrsim$98 keV b (or 119 keV b for an enhanced 3α rate). This is consistent with Aadland et al. (2022), who suggest that observations of WO-type Wolf–Rayet stars are best matched by models with a 25%–50% reduced $^{12}C(\alpha,\gamma)^{16}O$ rate.

5. Conclusions

Three physics-driven transitions in the BH initial mass function are predicted by single-star stellar evolution. We have have focused this work on the lower edge of the upper BH mass gap, the second transition. By evolving He cores from the He ZAMS to their final fate, we have explored physically motivated mixing floors, varying spatial and temporal resolutions, and a wide range of C/O core compositions to assess the numerical convergence of our MESA stellar evolution models. We find:

1. The inclusion of $D_{min} = 10^{-2}$ cm^2 s improves the rate of convergence of the models run with lower temporal resolution, but cannot fully recover the convective behavior generated by models that use higher temporal resolution.
2. The mass resolution needed to resolve the peak of the BH mass spectrum is limited by the amount of temporal resolution available. Models with high mass and low temporal resolutions smear out the BH mass spectrum peak. Models with lower mass and higher temporal resolutions display the largest overall peak BH mass. In MESA, time steps limited by $\delta_{\log \rho_c} \leqslant 2.5 \times 10^{-4}$ are needed to resolve the peak BH mass to within $\leqslant 1\,M_\odot$, and $\delta_{\log \rho_c} \leqslant 10^{-4}$ are needed to accurately resolve the shape of the BH mass spectrum.
3. By adopting resolutions of `5m_2h_10t` or `5m_2h_10t_D`, our peak BH mass models are robust to mass and temporal resolutions at the $\simeq$1% level at $\sigma[^{12}C(\alpha,\gamma)^{16}O] = 0$ and at the $\simeq$2% level across the mass gap. This resolution underestimates the peak BH mass by $\leqslant 2\,M_\odot$ at $\sigma = -3$ and overestimates the peak BH mass by $\leqslant 1\,M_\odot$ at $\sigma = 3$. The resolved lower edge shows reasonable agreement with the results of Mehta et al. (2022) at the $\leqslant 4\,M_\odot$ level across the lower edge of the BH mass gap. We establish a new lower edge of the upper mass gap as $M_{lower} \simeq 60^{+32}_{-14}\ M_\odot$, from the $\pm 3\sigma$ uncertainty in the $^{12}C(\alpha,\ \gamma)^{16}O$ reaction rate probability distribution function (Mehta et al. 2022).
4. At $\sigma[^{12}C(\alpha,\gamma)^{16}O] = -3$, the BH mass spectrum grows linearly with the initial He core mass, until the models explode as PISNe. If the true $^{12}C(\alpha,\gamma)^{16}O$ rate is in fact this weak, we do not expect to observe any $Z = 10^{-5}$

Table 2
MESA BH Mass Gap He Core Explosive Behavior for Figure 9

σ^{12}C (α, γ)	$M_{\rm He}$ ($M_\odot$)	$M_{\rm CO}$ ($M_\odot$)	X(^{12}C)	Pulses	$M_{\rm BH}$ ($M_\odot$)
$f_{3\alpha} = 1$					
−3.0	92	82.80	0.3156	0	91.45
−2.5	85	76.57	0.2816	1 weak	84.51
−2.0	80	72.12	0.2510	0	79.55
−1.5	73	72.61	0.2278	1 strong, ∼10 weak	71.84
−1.0	65	58.93	0.2105	>100 weak	64.41
−0.5	65	59.03	0.1855	1 strong, ∼10 weak	63.03
0	62	56.39	0.1673	1 strong, ∼10 weak	60.07
0.5	58	52.37	0.1508	1 strong, ∼9 weak	56.47
1.0	56	49.73	0.1280	4 strong, >100 weak	50.01
1.5	56	50.10	0.1160	3 strong, >80 weak	48.55
2.0	56	49.69	0.0972	3 strong, >30 weak	47.94
2.5	55	49.07	0.0840	3 strong, >30 weak	46.63
3.0	55	48.89	0.0729	3 strong, >20 weak	45.88
$f_{3\alpha} = 1.378$					
−3.0	104	93.70	0.3689	0	103.34
−2.5	96	86.49	0.3356	0	95.41
−2.0	90	81.07	0.3061	0	89.47
−1.5	85	76.58	0.2800	0	84.51
−1.0	81	73.04	0.2564	0	80.54
−0.5	76	68.60	0.2370	>90 weak	75.41
0	70	63.27	0.2216	1 strong, ∼9 weak	68.61
0.5	65	59.03	0.2057	1 strong, ∼9 weak	63.53
1.0	63	57.31	0.1877	1 strong, ∼9 weak	61.35
1.5	62	56.42	0.1700	1 strong, ∼10 weak	60.27
2.0	60	54.57	0.1553	1 strong, >100 weak	57.29
2.5	57	51.70	0.1437	2 strong, >20 weak	52.73
3.0	55	48.72	0.1274	2 strong, >100 weak	51.18

Note. All models are computed with `5m_2h_10t`. $M_{\rm CO}$ and X(^{12}C) are the C–O core mass and the central ^{12}C mass fraction at core He depletion, respectively.

PPISN stars, as the lower edge of the pair-instability strip is synchronous with the lower edge of the BH mass gap. At $\sigma[^{12}{\rm C}(\alpha,\gamma)^{16}{\rm O}] = 0$, the lower edge of the pair-instability strip is $M_{\rm He} \sim 47\,M_\odot$. At $\sigma[^{12}{\rm C}(\alpha,\gamma)^{16}{\rm O}] = +3$, our highest-resolution models (`2m_2h_25t`) indicate that the lower edge of the pair-instability strip could be as low as $M_{\rm He} \simeq 32\,M_\odot$, about $5\,M_\odot$ lower than at any other resolution. High temporal resolution is necessary to resolve the lower edge of the pair-instability strip for models with low C/O mass fractions.

5. Increased temporal resolution is important during the hydrodynamic phase, due to the tight coupling between the nuclear burning and time-dependent convection. The models with larger $^{12}{\rm C}(\alpha,\gamma)^{16}{\rm O}$ rates yield cores with low C/O mass fractions, which undergo stronger nuclear burning episodes and convection, and experience hundreds of pulses.
6. We explored stronger 3α reaction rates by implementing a 37.8% larger rate as a multiplicative factor on the currently adopted NACRE rate. At $\sigma[^{12}{\rm C}(\alpha,\gamma)^{16}{\rm O}] = -3,\ 0,\ +3$, adopting a stronger 3α rate results in an increase in the lower edge of the upper stellar mass gap of $M_{\rm BH} = 11.9$, 8.4, $5.3\,M_\odot$, respectively, yielding $M_{\rm lower} \simeq 69^{+34}_{-18}\ M_\odot$.

Future efforts to explore the resolved evolutions of PPISN stars and their BH mass spectra could consider coupling the temperature-dependent uncertainties in the $^{12}{\rm C}(\alpha,\gamma)^{16}{\rm O}$ and 3α rate probability distribution functions (e.g., Fields et al. 2018), larger nuclear reaction networks, and time-dependent convection models (Jermyn et al. 2022; Kupka et al. 2022) with variations in the prescriptions for wind-driven mass loss, angular momentum transport, convective core overshooting (Tanikawa et al. 2021; Vink et al. 2021), and binary interactions.

A goal of forthcoming low-energy nuclear experiments is to further reduce the uncertainty in the $^{12}{\rm C}(\alpha,\gamma)^{16}{\rm O}$ reaction rate probability distribution (deBoer et al. 2017; Smith et al. 2021; Aliotta et al. 2022). Partnering with this laboratory astrophysics quest are other avenues for placing astrophysical constraints on the $^{12}{\rm C}(\alpha,\gamma)^{16}{\rm O}$ reaction rate, from the period spectra of variable carbon–oxygen white dwarfs (Chidester et al. 2022), the lifetimes of He core-burning stars (Imbriani et al. 2001; Jones et al. 2015), and the surface abundances of WO-type Wolf–Rayet stars (Aadland et al. 2022).

We thank James Deboer for sharing the $^{12}{\rm C}\ (\alpha,\ \gamma)^{16}{\rm O}$ probability distribution function. This research is supported by the National Science Foundation (NSF) under grant No. PHY-1430152 for the "Joint Institute for Nuclear Astrophysics—Center for the Evolution of the Elements," and by the NSF under Software Infrastructure for Sustained Innovation grant Nos. ACI-1663684, ACI-1663688, and ACI-1663696 for the MESA Project. This research has made extensive use of the SAO/NASA Astrophysics Data System (ADS).

Software: MESA (Paxton et al. 2011, 2013, 2015, 2018, 2019; Jermyn et al. 2022; http://mesa.sourceforge.net), MESASDK 20190830 (Townsend 2019a, 2019b), `matplotlib` (Hunter 2007), and `NumPy` (van der Walt et al. 2011).

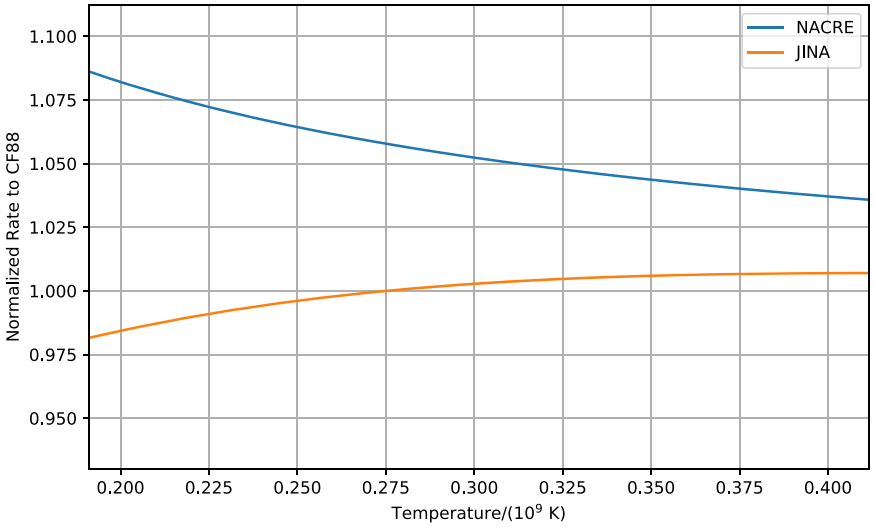

Figure 10. Normalized 3α reaction rates over core He burning temperatures 0.2–0.4 GK. Both the NACRE and JINA rates are normalized to the 3α rate from Caughlan & Fowler (1988; CF88).

Appendix

MESA tabulates nuclear reaction rates with a grid of 10,000 temperature points evenly spaced over 0–20 GK. Figure 10 illustrates MESA's implementation of both the NACRE and JINA 3α rates normalized to Caughlan & Fowler (1988; CF88) at He-burning temperatures.

ORCID iDs

Ebraheem Farag https://orcid.org/0000-0002-5794-4286
Mathieu Renzo https://orcid.org/0000-0002-6718-9472
Robert Farmer https://orcid.org/0000-0003-3441-7624
Morgan T. Chidester https://orcid.org/0000-0002-5107-8639
F. X. Timmes https://orcid.org/0000-0002-0474-159X

References

Aadland, E., Massey, P., John Hillier, D., et al. 2022, ApJ, 931, 157
Abbott, B. P., Abbott, R., Abbott, T. D., et al. 2017a, ApJ, 848, L12
Abbott, B. P., Abbott, R., Abbott, T. D., et al. 2017b, PhRvL, 119, 161101
Abbott, R., Abbott, T. D., Abraham, S., et al. 2020, ApJL, 896, L44
Acernese, F., Agathos, M., Agatsuma, K., et al. 2015, CQGra, 32, 024001
Akutsu, T., Ando, M., Arai, K., et al. 2021, PTEP, 2021, 05A102
Aliotta, M., Buompane, R., Couder, M., et al. 2022, JPhG, 49, 010501
Angulo, C., Arnould, M., Rayet, M., et al. 1999, NuPhA, 656, 3
Antoniadis, J., Freire, P. C. C., Wex, N., et al. 2013, Sci, 340, 448
Antonini, F., & Perets, H. B. 2012, ApJ, 757, 27
Austin, S. M., West, C., & Heger, A. 2014, PhRvL, 112, 111101
Bailyn, C. D., Jain, R. K., Coppi, P., & Orosz, J. A. 1998, ApJ, 499, 367
Banik, S., Hempel, M., & Bandyopadhyay, D. 2014, ApJS, 214, 22
Barkat, Z., Rakavy, G., & Sack, N. 1967, PhRvL, 18, 379
Bartos, I., Kocsis, B., Haiman, Z., & Marka, S. 2017, ApJ, 835, 165
Belczynski, K. 2020, ApJL, 905, L15
Belczynski, K., Wiktorowicz, G., Fryer, C. L., Holz, D. E., & Kalogera, V. 2012, ApJ, 757, 91
Bond, J. R., Arnett, W. D., & Carr, B. J. 1984, ApJ, 280, 825
Branch, D., & Wheeler, J. C. 2017, Supernova Explosions (Berlin: Springer)
Breivik, K., Coughlin, S., Zevin, M., et al. 2020, ApJ, 898, 71
Caughlan, G. R., & Fowler, W. A. 1988, ADNDT, 40, 283
Chidester, M. T., Farag, E., & Timmes, F. X. 2022, ApJ, 935, 21
Colpi, M., Shapiro, S. L., & Teukolsky, S. A. 1989, ApJ, 339, 318
Colpi, M., Shapiro, S. L., & Teukolsky, S. A. 1993, ApJ, 414, 717
Cook, K. J., Chevis, A., Eriksen, T. K., et al. 2021, PhRvC, 104, 024620
Costa, G., Bressan, A., Mapelli, M., et al. 2021, MNRAS, 501, 4514
Cromartie, H. T., Fonseca, E., Ransom, S. M., et al. 2020, NatAs, 4, 72
Cyburt, R. H., Amthor, A. M., Ferguson, R., et al. 2010, ApJS, 189, 240
de Mink, S. E., & Mandel, I. 2016, MNRAS, 460, 3545
deBoer, R. J., Gorres, J., Wiescher, M., et al. 2017, RvMP, 89, 035007
Di Carlo, U. N., Mapelli, M., Giacobbo, N., et al. 2020, MNRAS, 498, 495
Eriksen, T. K., Kibedi, T., Reed, M. W., et al. 2020, PhRvC, 102, 024320
Farmer, R., Fields, C. E., Petermann, I., et al. 2016, ApJS, 227, 22
Farmer, R., Renzo, M., de Mink, S. E., Fishbach, M., & Justham, S. 2020, ApJL, 902, L36
Farmer, R., Renzo, M., de Mink, S. E., Marchant, P., & Justham, S. 2019, ApJ, 887, 53
Farr, W. M., & Chatziioannou, K. 2020, RNAAS, 4, 65
Farr, W. M., Sravan, N., Cantrell, A., et al. 2011, ApJ, 741, 103
Fernandez, R., Quataert, E., Kashiyama, K., & Coughlin, E. R. 2018, MNRAS, 476, 2366
Ferreira, M., & Providencia, C. 2021, PhRvD, 104, 063006
Fields, C. E., Timmes, F. X., Farmer, R., et al. 2018, ApJS, 234, 19
Fonseca, E., Cromartie, H. T., Pennucci, T. T., et al. 2021, ApJL, 915, L12
Fowler, W. A., & Hoyle, F. 1964, ApJS, 9, 201
Fragione, G., Kocsis, B., Rasio, F. A., & Silk, J. 2022, ApJ, 927, 231
Fraley, G. S. 1968, Ap&SS, 2, 96
Freer, M., & Fynbo, H. O. U. 2014, PrPNP, 78, 1
Fryer, C., Benz, W., Herant, M., & Colgate, S. A. 1999, ApJ, 516, 892
Fryer, C. L., Belczynski, K., Wiktorowicz, G., et al. 2012, ApJ, 749, 91
Fryer, C. L., Olejak, A., & Belczynski, K. 2022, ApJ, 931, 94
Fryer, C. L., Woosley, S. E., & Heger, A. 2001, ApJ, 550, 372
Fuller, J., & Lu, W. 2022, MNRAS, 511, 3951
Ghosh, S., Wolfe, N., & Frohlich, C. 2022, ApJ, 929, 43
Glatzel, W., Fricke, K. J., & El Eid, M. F. 1985, A&A, 149, 413
Gupta, A., Gerosa, D., Arun, K. G., et al. 2020, PhRvD, 101, 103036
Haensel, P., Zdunik, J. L., & Douchin, F. 2002, A&A, 385, 301
Hamers, A. S., & Samsing, J. 2019, MNRAS, 487, 5630
Heger, A., Fryer, C. L., Woosley, S. E., Langer, N., & Hartmann, D. H. 2003, ApJ, 591, 288
Higgins, E. R., Sander, A. A. C., Vink, J. S., & Hirschi, R. 2021, MNRAS, 505, 4874
Hoyle, F. 1954, ApJS, 1, 121
Hunter, J. D. 2007, CSE, 9, 90
Imbriani, G., Limongi, M., Gialanella, L., et al. 2001, ApJ, 558, 903
Ivanov, M., & Fernandez, R. 2021, ApJ, 911, 6
Jacobson-Galan, W. V., Dessart, L., Jones, D. O., et al. 2022, ApJ, 924, 15
Jermyn, A. S., Bauer, E. B., Schwab, J., et al. 2022, arXiv:2208.03651
Jones, S., Hirschi, R., Pignatari, M., et al. 2015, MNRAS, 447, 3115
Kibedi, T., Alshahrani, B., Stuchbery, A. E., et al. 2020, PhRvL, 125, 182701
Koliogiannis, P. S., & Moustakidis, C. 2021, ApJ, 912, 69
Kunz, R., Fey, M., Jaeger, M., et al. 2002, ApJ, 567, 643
Kupka, F., Ahlborn, F., & Weiss, A. 2022, arXiv:2207.12296
Lattimer, J. M. 2021, ARNPS, 71, 433
LIGO Scientific Collaboration, Aasi, J., Abbott, B. P., et al. 2015, CQGra, 32, 074001
Liu, B., & Lai, D. 2018, ApJ, 863, 68

Mandel, I., & Broekgaarden, F. S. 2022, LRR, 25, 1
Mandel, I., & Farmer, A. 2022, PhR, 955, 1
Mapelli, M. 2021, in Handbook of Gravitational Wave Astronomy, ed. C. Bambi, S. Katsanevas, & K. D. Kokkotas (Singapore: Springer), 16
Marchant, P., & Moriya, T. J. 2020, A&A, 640, L18
Marchant, P., Renzo, M., Farmer, R., et al. 2019, ApJ, 882, 36
Marques, M., Oertel, M., Hempel, M., & Novak, J. 2017, PhRvC, 96, 045806
Matzner, C. D., & Ro, S. 2021, ApJ, 908, 23
Mehta, A. K., Buonanno, A., Gair, J., et al. 2022, ApJ, 924, 39
Miller, M. C., Lamb, F. K., Dittmann, A. J., et al. 2021, ApJL, 918, L28
Nadyozhin, D. K. 1980, Ap&SS, 69, 115
Nixon, C. J., Coughlin, E. R., & Pringle, J. E. 2020, ApJL, 900, L12
Nomoto, K., Thielemann, F.-K., & Miyaji, S. 1985, A&A, 149, 239
Ober, W. W., El Eid, M. F., & Fricke, K. J. 1983, A&A, 119, 61
O'Leary, R. M., Kocsis, B., & Loeb, A. 2009, MNRAS, 395, 2127
Oppenheimer, J. R., & Serber, R. 1938, PhRv, 54, 540
Ozel, F., Psaltis, D., Narayan, R., & McClintock, J. E. 2010, ApJ, 725, 1918
Page, D. N. 1982, PhLA, 91, 201
Patton, R. A., & Sukhbold, T. 2020, MNRAS, 499, 2803
Patton, R. A., Sukhbold, T., & Eldridge, J. J. 2022, MNRAS, 511, 903
Paxton, B., Bildsten, L., Dotter, A., et al. 2011, ApJS, 192, 3
Paxton, B., Cantiello, M., Arras, P., et al. 2013, ApJS, 208, 4
Paxton, B., Marchant, P., Schwab, J., et al. 2015, ApJS, 220, 15
Paxton, B., Schwab, J., Bauer, E. B., et al. 2018, ApJS, 234, 34
Paxton, B., Smolec, R., Schwab, J., et al. 2019, ApJS, 243, 10
Perna, R., Wang, Y.-H., Farr, W. M., Leigh, N., & Cantiello, M. 2019, ApJL, 878, L1
Portegies Zwart, S. F., & McMillan, S. L. W. 2000, ApJL, 528, L17
Quataert, E., & Shiode, J. 2012, MNRAS, 423, L92
Rahman, N., Janka, H.-T., Stockinger, G., & Woosley, S. E. 2022, MNRAS, 512, 4503
Rakavy, G., & Shaviv, G. 1967, ApJ, 148, 803
Renzo, M., Cantiello, M., Metzger, B. D., & Jiang, Y. F. 2020a, ApJL, 904, L13
Renzo, M., Farmer, R., Justham, S., et al. 2020b, A&A, 640, A56
Renzo, M., Farmer, R. J., Justham, S., et al. 2020c, MNRAS, 493, 4333
Renzo, M., Hendriks, D. D., van Son, L. A. C., & Farmer, R. 2022, RNAAS, 6, 25
Renzo, M., Ott, C. D., Shore, S. N., & de Mink, S. E. 2017, A&A, 603, A118
Renzo, M., Callister, T., Chatziioannou, K., et al. 2021, ApJ, 919, 128
Rezzolla, L., Most, E. R., & Weih, L. R. 2018, ApJL, 852, L25
Richers, S., Ott, C. D., Abdikamalov, E., O?Connor, E., & Sullivan, C. 2017, PhRvD, 95, 063019
Riley, T. E., Watts, A. L., Ray, P. S., et al. 2021, ApJL, 918, L27
Rolfs, C. E., & Rodney, W. S. 1988, Theoretical Astrophysics (Chicago, IL: Univ. Chicago Press)
Sallaska, A. L., Iliadis, C., Champange, A. E., et al. 2013, ApJS, 207, 18
Sana, H., & Evans, C. J. 2011, in IAU Symp. 272, Active OB Stars: Structure, Evolution, Mass Loss, and Critical Limits, ed. C. Neiner et al. (Cambridge: Cambridge Univ. Press), 474
Sana, H., de Mink, S. E., de Koter, A., et al. 2012, Sci, 337, 444
Santoliquido, F., Mapelli, M., Giacobbo, N., Bouffanais, Y., & Artale, M. C. 2021, MNRAS, 502, 4877
Schwab, J. 2021, ApJ, 906, 53
Shiode, J. H., & Quataert, E. 2014, ApJ, 780, 96
Siegel, D. M., Agarwal, A., Barnes, J., et al. 2021, arXiv:2111.03094
Smith, R., Gai, M., Stern, S. R., Schweitzer, D. K., & Ahmed, M. W. 2021, NatCo, 12, 5920
Spera, M., Mapelli, M., & Bressan, A. 2015, MNRAS, 451, 4086
Spera, M., Mapelli, M., Giacobbo, N., et al. 2019, MNRAS, 485, 889
Spera, M., Trani, A. A., & Mencagli, M. 2022, Galax, 10, 76
Stothers, R. B. 1999, MNRAS, 305, 365
Sukhbold, T., Ertl, T., Woosley, S. E., Brown, J. M., & Janka, H.-T. 2016, ApJ, 821, 38
Sukhbold, T., Woosley, S. E., & Heger, A. 2018, ApJ, 860, 93
Sumiyoshi, K., Yamada, S., Suzuki, H., & Hillebrandt, W. 1998, A&A, 334, 159
Takahashi, K. 2018, ApJ, 863, 153
Tanikawa, A., Kinugawa, T., Yoshida, T., Hijikawa, K., & Umeda, H. 2021, MNRAS, 505, 2170
The LIGO Scientific Collaboration, the Virgo Collaboration, the KAGRA Collaboration, et al. 2021, arXiv:2111.03634
Thompson, T. A., Kochanek, C. S., Stanek, K. Z., et al. 2019, Sci, 366, 637
Timmes, F. X., Woosley, S. E., & Weaver, T. A. 1996, ApJ, 457, 834
Toro, E. F., Spruce, M., & Speares, W. 1994, ShWav, 4, 25
Townsend, R. H. D. 2019a, MESA SDK for Linux20190503 v20190503, Zenodo, doi:10.5281/zenodo.2669541
Townsend, R. H. D. 2019b, MESA SDK for Mac OS v20190503, Zenodo, doi:10.5281/zenodo.2669543
Uchida, H., Shibata, M., Takahashi, K., & Yoshida, T. 2019, ApJ, 870, 98
van der Walt, S., Colbert, S. C., & Varoquaux, G. 2011, CSE, 13, 22
van Son, L. A. C., De Mink, S. E., Broekgaarden, F. S., et al. 2020, ApJ, 897, 100
Vink, J. S., Higgins, E. R., Sander, A. A. C., & Sabhahit, G. N. 2021, MNRAS, 504, 146
Vink, J. S., Heger, A., Krumholz, M. R., et al. 2015, HiA, 16, 51
Wang, B., Liu, D., & Chen, H. 2022, MNRAS, 510, 6011
Wang, H., Stephan, A. P., Naoz, S., Hoang, B.-M., & Breivik, K. 2021, ApJ, 917, 76
West, C., Heger, A., & Austin, S. M. 2013, ApJ, 769, 2
Woosley, S. E. 2017, ApJ, 836, 244
Woosley, S. E. 2019, ApJ, 878, 49
Woosley, S. E., & Heger, A. 2021, ApJL, 912, L31
Woosley, S. E., Heger, A., & Weaver, T. A. 2002, RvMP, 74, 1015
Wu, S. C., & Fuller, J. 2022, ApJ, 930, 119
Wyrzykowski, Ł., & Mandel, I. 2020, A&A, 636, A20
Yang, Y., Gayathri, V., Bartos, I., et al. 2020, ApJL, 901, L34
Ye, C., & Fishbach, M. 2022, arXiv:2202.05164
Yoshida, T., Umeda, H., Maeda, K., & Ishii, T. 2016, MNRAS, 457, 351
Zapartas, E., Renzo, M., Fragos, T., et al. 2021, A&A, 656, L19
Zevin, M., Spera, M., Berry, C. P. L., & Kalogera, V. 2020, ApJL, 899, L1
Zevin, M., Bavera, S. S., Berry, C. P. L., et al. 2021, ApJ, 910, 152
Zhang, W., Woosley, S. E., & Heger, A. 2008, ApJ, 679, 639